

Autonomous methane seep site monitoring offshore Western Svalbard: Hourly to seasonal variability and associated oceanographic parameters

Knut Ola Dølven¹, Bénédicte Ferré¹, Anna Silyakova¹, Pär Jansson^{2,*}, Peter Linke^{3,*}, and Manuel Moser^{1,*}

¹Centre for Arctic Gas Hydrate, Environment, and Climate, UiT The Arctic University of Norway, 9019 Tromsø, Norway

²Multiconsult Kyst og Marin, 9013 Tromsø, Norway

³GEOMAR Helmholtz Centre for Ocean Research Kiel, 24148 Kiel, Germany

*These authors contributed equally to this work

Correspondence: Knut Ola Dølven (knut.o.dolven@uit.no)

Abstract. Improved quantification techniques of natural sources are needed to explain variations in atmospheric methane. In polar regions, high uncertainties in current estimates of methane release from the seabed remain. We present two unique 10 and 3 months long time-series of bottom water measurements of physical and chemical parameters from two autonomous ocean observatories deployed at separate intense seabed methane seep sites (91 and 246 m depth), offshore Western Svalbard from 5 2015 to 2016. Results show high short term (100-1000 nmol L⁻¹ within hours) and seasonal variation, as well as higher (2-7 times) methane concentrations compared to previous measurements. Rapid variability is explained by uneven distribution of seepage and changing ocean current directions. No overt influence of tidal hydrostatic pressure or water temperature variations on methane concentration was observed, but an observed negative correlation with temperature at the 246 m site fits with 10 hypothesized seasonal blocking of lateral methane pathways in the sediments. Negative correlation between bottom water methane concentration/variability and wind forcing, concomitant with signs of weaker water column stratification indicates increased potential for methane release to the atmosphere in fall/winter. We present new information about short- and long-term methane variability and provide a preliminary constraint on the uncertainties that arise in methane inventory estimates from this variability.

1 Introduction

15 Unexplained changes in atmospheric methane (CH₄) mole fraction motivates research in understanding and quantifying non-anthropogenic sources (Saunio et al., 2020). The atmospheric forcing of CH₄ is particularly sensitive to changes in emission rates due to a high warming potential and short lifetime. Improved knowledge about atmospheric CH₄ fluxes is therefore crucial to constrain future climate projections (Pachauri and Meyer, 2014; Myhre et al., 2016b). These properties of atmospheric CH₄ also makes reduced anthropogenic CH₄ emissions a potential solution for rapid climate change mitigation (Saunio et al., 20 2016). A global effort to cut greenhouse gas emissions through international agreements is, however, dependent on precise estimates of sources and sinks to verify contributions from different nations.

Seabed seepage is considered a minor source of atmospheric CH₄, but with high uncertainty in current and predicted emission estimates (Saunois et al., 2016). Current estimates suggest a total contribution of 7 (5-10) Tg y⁻¹ (Etioppe et al., 2019; Saunois et al., 2020), which is ~1% of the total CH₄ emissions to the atmosphere. Methane is released from the seabed as free gas (bubbles) and dissolved gas in sediment pore water. Bubbles rise quickly towards the sea surface, but most CH₄ dissolves near the seafloor because of gas exchange across the bubble rims and bubble dissolution (McGinnis et al., 2006; Jansson et al., 2019a). Dissolved CH₄ is dispersed and advected by ocean currents (Silyakova et al., 2020) and is continuously transformed to carbon dioxide (CO₂) by bacterial aerobic oxidation (Hanson and Hanson, 1996; Reeburgh, 2007). These processes significantly limit the lifetime of CH₄ in the water column and the amount of CH₄ that can reach the atmosphere is highly dependent on the depth where the seepage occurs (McGinnis et al., 2006; Graves et al., 2015). Intense CH₄ seepage at shallow depths in coastal areas and on continental shelves is therefore the main potential source of seabed CH₄ to the atmosphere.

The shallow continental margins of the Arctic Ocean store large amounts of CH₄ as free gas, gas dissolved in pore water fluid, and gas hydrates (James et al., 2016; Ruppel and Kessler, 2017), i.e. clathrate structures composed of water trapped by hydrocarbon molecules formed and kept stable at low temperature and high pressure (Sloan, 1998). Methane trapped in hydrates or in subsea permafrost, as well as hydrate sealed free gas reservoirs can be destabilized by increasing bottom water temperature, resulting in a potential positive climate feedback loop (Westbrook et al., 2009; Shakhova et al., 2010; James et al., 2016).

Studies on CH₄ inventory, distribution and release in the Arctic Ocean are mainly based on research cruise data from late spring to early fall, when ice and weather conditions allow field work in the region (Gentz et al., 2014; Sahling et al., 2014; Mau et al., 2017), whereas winter data is sparse. Bottom water temperature (Westbrook et al., 2009; Reagan et al., 2011; Ferré et al., 2012; Braga et al., 2020), water mass origins (Steinle et al., 2015), micro-seismicity (Franek et al., 2017), and hydrostatic pressure (Linke et al., 2009; Römer et al., 2016) have all been proposed to be linked with sources and sinks of CH₄ in the water column. These processes act on a wide range of time-scales, from hours (e.g. hydrostatic pressure) to decades (bottom water temperature). Without a better understanding of the spatial and temporal variability of CH₄ in Arctic Seep sites, it is challenging to untangle these processes. Unconstrained local variability in CH₄ seepage and concentration also imposes a high degree of uncertainty on CH₄ inventory estimates (Saunois et al., 2020). The combination of climate sensitive CH₄ storages, vast shallow ocean regions and limited data availability highlight the need for more understanding of seabed CH₄ seepage on Arctic shelves.

To assess the aforementioned challenges, we have obtained, analyzed and compared unique year-round underwater multi-parameter time series from two seafloor observatories deployed at two intense CH₄ seep sites on the western Svalbard continental shelf (Figure 1) where no CH₄ measurements have previously been done in winter season. We combine high frequency physical (ocean currents, temperature, salinity, pressure) and chemical (O₂, CO₂, CH₄) data to perform hypothesis testing and provide new insights on CH₄ distribution, content, as well as variability on short (minutes) and long (seasonal) timescales and potential implications.

55 1.1 Regional Settings

Two observatories (O_{91} and O_{246}) were deployed from June 2015 (CAGE 15-3 cruise) to May 2016 (CAGE 16-4 cruise) from R/V *Helmer Hanssen* at the inter-trough shelf region between Isfjorden and Kongsfjorden, west of Prins Karls Forland (PKF). The O_{91} observatory was deployed at 91 m water depth on the continental shelf (78.561°N, 10.142°E) and the O_{246} observatory was deployed at 246 m water depth further offshore close to the shelf break (78.655°N, 9.433°E, Figure 1).

60 Both sites were located in areas with thousands of previously mapped CH_4 gas seeps (e.g. Sahling et al. (2014); Veloso-Alarcón et al. (2019); Silyakova et al. (2020); this work, see Figure 1), often referred as "flares" due to the appearance of bubble streams in echo-sounder data. Nonetheless, atmospheric sampling in this region suggests that any emissions to the atmosphere are small (Platt et al., 2018). Gas accumulation at the O_{246} seep site has been suggested to be a result of gas migration in permeable layers within the seabed from deeper free gas or hydrate reservoirs (Rajan et al., 2012; Sarkar et al., 2012; Veloso-
65 Alarcón et al., 2019), while seepage at site O_{91} has been attributed to thawing sub-sea permafrost due to ice sheet retreat at the end of the last glaciation (Sahling et al., 2014; Portnov et al., 2016). Water sampling have indicated high temporal variability with bottom water concentrations (average) changing from 200 nmol L^{-1} within 1 week in July 2014 at O_{91} (Myhre et al., 2016a) and $\sim 80 \text{ nmol L}^{-1}$ within 20 hours (two single point measurements) at O_{246} in August 2010 (Gentz et al., 2014). A consistent pattern of decreasing concentrations from the sea floor to the sea surface at both sites (400 to $<8 \text{ nmol L}^{-1}$ at
70 O_{91} (Myhre et al., 2016a)) and from to >500 to $<20 \text{ nmol L}^{-1}$ at O_{246} (Gentz et al., 2014)) has also been observed. Further offshore, continuous measurements from a towed fast-response underwater laser spectrometer also revealed very high spatial CH_4 variability (Jansson et al., 2019b).

The local water masses are characterized by exchange and convergence of the warm, saline Atlantic Water (AW, Temperature $T > 3^\circ\text{C}$ and absolute salinity $S_A > 34.65$) in the West Spitsbergen Current (WSC) (Beszczynska-Möller et al., 2012) and the
75 colder, fresher Arctic Water (ArW, $-1.5 < T < 1^\circ\text{C}$, $34.3 < S_A < 34.8$) in the Coastal Current (CC) (Hopkins, 1991) combined with seasonal cooling, ice formation, and freshwater input from land (Nilsen et al., 2016) (Figure 1). Local mixing rates can be strongly affected by synoptic scale weather systems, causing upwelling and disruption of the front between the two ocean currents (Saloranta and Svendsen, 2001; Cottier et al., 2007). Freshwater input in summer stratifies the water column, while cooling, storm activity and sea ice formation can facilitate vertical mixing in winter (Saloranta and Svendsen, 2001; Nilsen
80 et al., 2016).

2 Methods

The "K-Lander" ocean observatories were designed to monitor CH_4 release and associated physical and chemical parameters in challenging environments (see Appendix A). A launcher equipped with camera and telemetry allowed for safe deployment at a site selected by visual control. Observatory O_{91} recorded data from 2 July 2015 to 6 May 2016, while O_{246} recorded data
85 from 1 July until 3 October 2015, when data recording ceased due to an electrical malfunction.

Both observatories were equipped with an Acoustic Doppler Current Profiler (ADCP), a CTD with oxygen optode, and Contros HydroC CO_2 II and HydroC *Plus* CH_4 sensors (Figure A1a, details in Appendix B). The CH_4 sensors rely on a

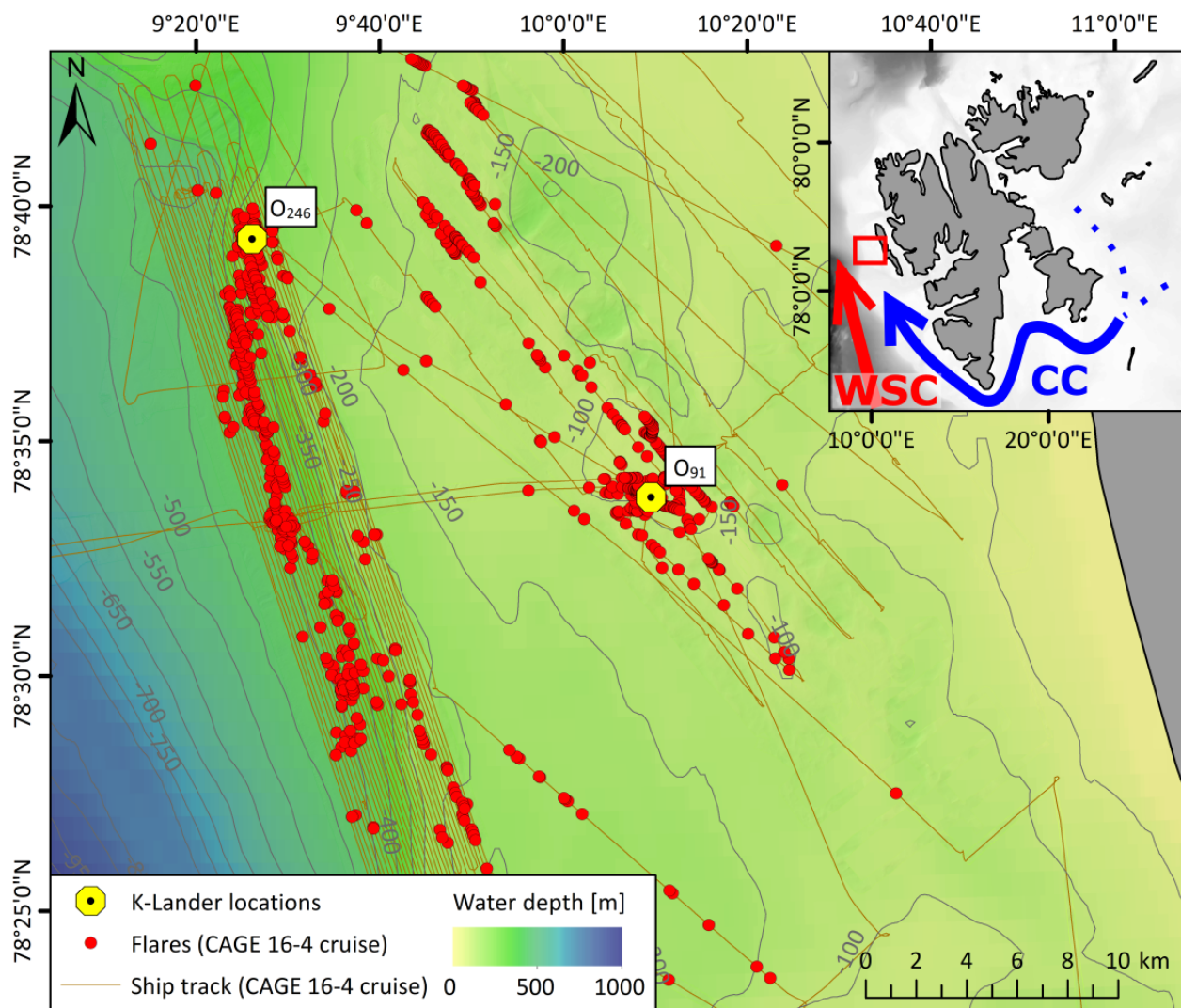


Figure 1. Bathymetry of the study area with location of the observatories O₉₁ and O₂₄₆ offshore western Svalbard. Flares detected by single-beam echo sounder survey prior to recovering the observatories (May 2016, cruise CAGE 16-4) are indicated with red dots and ship tracks as brown lines. The inset map shows the working area (red square) offshore Svalbard. WSC and CC refer to the warm West Spitsbergen Current and cold Coastal Current, respectively.

Tunable Diode Laser Absorption Spectrometry (TDLAS) detector, while the CO₂ sensors use Non-dispersive infrared (NDIR) detectors. Both sensors were equipped with polydimethylsiloxate (PDMS) membranes, and a Seabird SBE 5M pump (see Appendix B). Detailed description of general post-processing, technical features of the data and measurement accuracies are outlined in Appendix B.

We calculated correlation coefficient (R) matrices to give a first order overview of linear relationships between the measured parameters. We mapped the flares in the area using single-beam echo-sounder data collected during the observatory recovery cruise in 2016 (CAGE 16-4, Figure 1) and estimated gas flow rates using the FlareHunter software (Veloso et al., 2015). Additionally, we obtained 10 m wind reanalysis data from the ERA-Interim database.

We calculated seawater density (McDougall and Barker, 2011) and CH₄ solubility (Kossel et al., 2013) using the CTD data. A CTD cast (SBE plus 24 Hz) prior to the O₉₁ recovery (6 May, 2016) showed a salinity drift in the conductivity sensor of around -0.4 (here and elsewhere in the paper, salinity values are practical salinity). Post-calibration, inspection of the conductivity signal and potential water mass mixing end-members indicates that this might have been caused by mud pollution occurring in late 2015 or early 2016.

High power consumption of the Contros HydroC CH₄ and CO₂ sensors required a power cycling mode to allow for long-term monitoring while simultaneously capturing rapid short-term variability. Partial pressure of CH₄ and CO₂ was therefore measured continuously for 24 hours every 21 days, and for one hour every day (see Table B1). Methane concentration data were corrected for slow response time following Dølven et al., (2021) onto a 3 minute interval grid and converted to absolute concentration, which is the default "CH₄ concentration" discussed and described in this text. Uncertainty ranges for the CH₄ data are reported as 95% confidence intervals and typically vary between 5 and 20% (full distribution of uncertainties are in Figure B1b). Faulty pumps in the CO₂ sensors ambiguously increased the response time which prevented response time correction, making CO₂ data suitable only for long-term qualitative analysis.

3 Results

3.1 Time series at site O₉₁

Dissolved CH₄ concentration at site O₉₁ ranged from 5±3 nmol L⁻¹ (6 December in 2015) to 1748±142 nmol L⁻¹ (20 August in 2015) (Figure 2a and Appendix C), with 2.5 and 97.5 percentiles of 16 and 785 nmol L⁻¹. The data follows a nearly log-normal distribution, with a mean and median of 227 and 165 nmol L⁻¹, respectively, and interquartile range of 88-334 nmol L⁻¹. Large variations (>100 up to almost 1000 nmol L⁻¹) in CH₄ concentration occurred on short time-scales (<1 hour) throughout the measurement period (see Figure 2a, d, and all 24-hour periods in Appendix C) with an average range for all the 24-hour periods of 840 nmol L⁻¹ and median rate of change (ROC) of 3.2 nmol L⁻¹ min⁻¹. We also observe a long-term trend of decreasing running median (2-week window) concentrations towards winter, from 495 nmol L⁻¹ in July/August 2015 to 53 nmol L⁻¹ in January 2016 (Figure 2). There was a relatively weak, but significant negative correlation between the wind speed and CH₄ concentration (R_{RTC}=-0.33), but otherwise weak to non-existent linear relationships between CH₄ concentration and the measured ocean parameters (Table 1).

Table 1. Correlation coefficients between variables at O₉₁. "RTC CH₄" and "Raw CH₄" refers to response time corrected and untreated CH₄ data, respectively (Sect. 2 and Appendix B). Units used are mol L⁻¹, °C, salinity, mol L⁻¹, dbar, mol L⁻¹, m s⁻¹, and μatm for dissolved CH₄, temperature, PSU, dissolved oxygen, pressure, CH₄ solubility, wind speed, and partial pressure of CO₂, respectively.

	RTC CH ₄	Raw CH ₄	Temperature	Salinity	Oxygen	Pressure	Solubility	Wind speed	CO ₂
RTC CH ₄	1	0.91	-0.06	0.23	0.03	0.08	0.06	-0.33	-0.25
Raw CH ₄	0.91	1	-0.07	0.27	0.03	0.10	0.06	-0.37	-0.31
Temperature	-0.06	-0.07	1	0.69	-0.94	-0.01	-0.99	0.37	0.29
Salinity	0.23	0.27	0.69	1	-0.78	-0.06	-0.58	0.06	0.46
Oxygen	0.03	0.03	-0.94	-0.78	1	0.02	0.85	-0.33	-0.67
Pressure	0.08	0.10	-0.01	-0.06	0.02	1	0.16	0.00	-0.10
Solubility (CH ₄)	0.06	0.06	-0.99	-0.58	0.85	0.16	1	-0.35	-0.30
Wind speed	-0.33	-0.37	0.37	0.06	-0.33	0.00	-0.35	1	0.52
CO ₂	-0.25	-0.31	0.29	0.46	-0.67	-0.10	-0.30	0.52	1

CO₂ averaged 403 μatm with an increase towards mid-November 2015 (~410 μatm) then a decrease until 6 May (~391 μatm) in 2016 (Figure 2a). CO₂ dropped to ~305 μatm on 24 August, concurrent with a rapid decrease in salinity (-0.5), increase in temperature and oxygen, and high CH₄ concentration. The increase in oxygen rules out methanogenesis. Instead, there might be at least two explanations for the reduction of CO₂ and enrichment of CH₄: i) water column mixing brings oxygen-rich, warm and fresh surface water to deeper depth, and with it CO₂ depleted water or ii) methane enrichment by zooplankton following the summer bloom.

Bottom water temperature increased steadily from ~3 in July to ~5.5 °C in October/November 2015, with occasional sharp shifts (T±1°C) occurring within hours to days (Figure 2b). Temperature then decreased from the beginning of December to ~1.8°C at the end of the deployment in May 2016, showing more frequent and stronger episodes of rapid temperature shifts (T±2°C also occurring on hours-days). Despite uncertainty in salinity data, it is worth noting that these rapid shifts in temperature and salinity were reproduced by the Svalbard 800 model in the same area (Silyakova et al., 2020) by eddy activity.

Hydrostatic pressure was mostly governed by tides (94.5% of variance) with dominant semi-diurnal M2 tide (M2 refers to a tidal constituent with period 12.42 hours, see e.g. Gerkema (2019)). Amplitudes varied from ~1.2 to 1.5 meter during neap and spring cycles (Figure 2c).

The calculated CH₄ solubility decreased from 0.016 mol L⁻¹ in July to 0.015 mol L⁻¹ in the end of November 2015, and increased to almost 0.017 mol L⁻¹ in May 2016 (Figure 2c). This long-term trend was mainly caused by temperature variability (R=-0.99), while tidal pressure changes caused a semi-diurnal variation of ± ~0.005 mol L⁻¹.

Dissolved O₂ decreased from ~385 μmol L⁻¹ in July 2015 to ~350 μmol L⁻¹ at the beginning of December, and increased to ~400 μmol L⁻¹ towards 6 May, 2016 (Figure 2d) and followed temperature inversely (R=-0.94), with similar long and short-term variability.

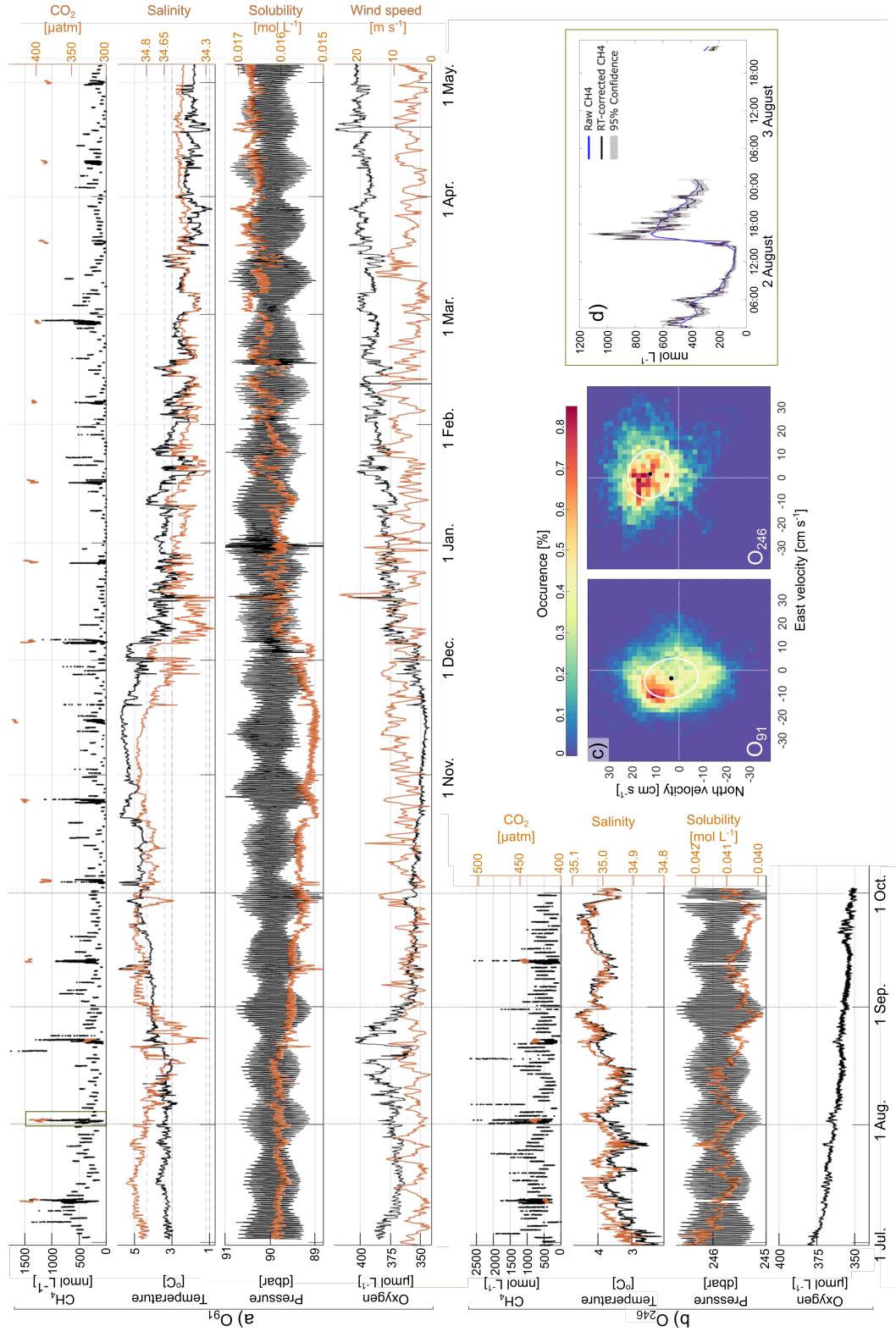


Figure 2. Time series from a) O₉₁ and b) O₂₄₆ showing response time corrected (see Appendix B) CH₄, CO₂, temperature, salinity, pressure, CH₄ solubility, oxygen, and wind speed (10 m) data. The O₂₄₆ data is truncated due to an electrical malfunction in the system on 3 October c) 2-d histogram and 1 standard deviation variance ellipse of bottom current velocity (81 m depth at O₉₁ and 236 m depth at O₂₄₆) and d) example of 24-hour and 1-hour (2 and 3 August) CH₄ concentration measurement period from O₉₁ (green box). All 24-hour measurement periods are shown in Appendix C. Note different scales between O₉₁ and O₂₄₆.

The averaged bottom water current (81 m above the seafloor) was 4 cm s^{-1} in a northwestward direction (321°N) (Figure 2c). The current usually had one anti-clockwise rotation every 23.93 hour period, corresponding to the diurnal K1 tidal constituent (tide with period 23.93 hours, see Gerkema (2019)) with a secondary semi-diurnal (M2) modulation.

3.2 Time series at site O₂₄₆

145 CH₄ concentration at site O₂₄₆ ranged from $10 \pm 3 \text{ nmol L}^{-1}$ on 21 September, 2015 to $2727 \pm 182 \text{ nmol L}^{-1}$ on 18 August 2015, with 2.5 and 97.5 percentiles of 107 and 1374 nmol L^{-1} . The data approximately follows log-normal distribution with average and median of 577 and 600 nmol L^{-1} , respectively, and interquartile range of $293\text{--}721 \text{ nmol L}^{-1}$. The median RoC of CH₄ was almost 20 times higher compared to site O₉₁ with $31 \text{ nmol L}^{-1} \text{ min}^{-1}$ (Figure 2b and Appendix C). There was also clear diurnal periodicity in CH₄ concentration at O₂₄₆. The long-term trend (2-week running mean) shows decreasing
150 concentrations until 3 October 2015 (end of the measuring period, Figure 2b). Dissolved O₂ decreased from $\sim 380 \mu\text{mol L}^{-1}$ to $\sim 300 \mu\text{mol L}^{-1}$ and was negatively correlated with water temperature ($R = -0.61$, see Table 2 for complete correlation matrix).

Table 2. Correlation coefficients between variables at O₉₁. "RTC CH₄" and "Raw CH₄" refers to response time corrected and untreated CH₄ (see Sect. 2 and Appendix B). Units used are mol L^{-1} , °C, salinity, mol L^{-1} , dbar, mol L^{-1} , m s^{-1} , and μatm for dissolved CH₄, temperature, PSU, dissolved oxygen, pressure, CH₄ solubility, wind speed, and partial pressure of CO₂, respectively.

	RTC CH ₄	Raw CH ₄	Temperature	Salinity	Oxygen	Pressure	Solubility	Wind speed	CO ₂
RTC CH ₄	1	0.78	-0.31	-0.24	0.30	0.15	0.33	-0.29	-0.13
Raw CH ₄	0.78	1	-0.45	0.26	0.48	0.10	0.45	-0.44	-0.09
Temperature	-0.31	-0.45	1	0.87	-0.61	-0.02	-0.99	0.38	0.22
Salinity	-0.24	-0.26	0.87	1	-0.22	-0.03	-0.87	0.07	0.13
Oxygen	0.30	0.48	-0.61	-0.22	1	0.06	0.59	-0.65	-0.41
Pressure	0.15	0.01	-0.02	-0.03	0.06	1	0.16	-0.05	0.14
Solu (CH ₄)	0.33	0.45	-0.99	-0.87	0.59	0.16	1	0.38	-0.20
Wind speed	-0.29	-0.44	0.38	0.07	-0.65	-0.05	0.38	1	0.18
CO ₂	-0.13	-0.09	0.22	0.13	-0.41	0.14	-0.20	0.41	1

Temperature and salinity increased from ~ 2.5 to ~ 4.0 °C and ~ 34.85 up to ~ 35.0 , respectively, from the deployment until October 2015 (Figure 2b), with AW dominance throughout the measuring period. Rapid shifts of around $\pm 1^\circ\text{C}$ and 0.05 salinity occurred occasionally over a period of hours to days.

155 Variance in hydrostatic pressure was mainly explained by the tides (95.2%) which was mainly governed by the semi-diurnal M2 tide, with weaker diurnal and fortnightly modulation (Figure 2b). Changes in pressure varied from ~ 1.2 to ~ 1.5 m during periods of neap and spring tide.

Being governed mainly by temperature ($R=-0.99$), CH_4 solubility dropped from 0.042 mol L^{-1} to 0.040 mol L^{-1} from the deployment in July until October 2015, with a semi-diurnal variation of $\sim 0.005 \text{ mol L}^{-1}$ due to tidal changes in hydrostatic
160 pressure.

The averaged current was $\sim 10 \text{ cm s}^{-1}$ northward (7°N) (Figure 2c). Variability in the along-slope current (direction -10°N) was strongly related to the semi-diurnal M2 tidal component, while the cross-slope currents were governed by the diurnal K1 frequency. The bottom water current rotated counterclockwise with a period of 23.93 hours (K1 tidal constituent), with semi-diurnal modulation in the along-slope component. Dissolved CH_4 concentration was weakly anti-correlated with wind
165 speed ($R=-0.29$), temperature ($R=-0.31$), salinity ($R=-0.24$), and positively correlated with CH_4 solubility ($R=0.33$) and oxygen ($R=0.3$).

4 Discussion

4.1 CH_4 variability

Combining mapped flares and flow rates from the recovery cruise (May 2016) with bottom water current velocity (9 meters
170 above the seafloor) reveals that CH_4 concentration was strongly affected by whether water was advected from areas where we mapped strong or weak seepage in May 2016 (Figure 3). Strong seeps (flow rate $>200 \text{ mL}^{-1} \text{ min}^{-1}$) were mainly located between ~ 30 and 80 m to the north/northeast of site O_{91} and only weak and more distant seepage was observed south-west of the observatory (Figure 3a). Consequently, averaged CH_4 concentration from water coming from north-east was $\sim 440 \text{ nmol L}^{-1}$, while water from south-west averaged $\sim 100 \text{ nmol L}^{-1}$. Similarly, a strong CH_4 seep (flow rate $\sim 1200 \text{ mL min}^{-1}$) was
175 mapped $\sim 40 \text{ m}$ north of site O_{246} , making water advected from this direction highly elevated in CH_4 with an average of $\sim 1400 \text{ nmol L}^{-1}$ compared to the overall average of 577 nmol L^{-1} (Figure 3b). The rapid changes in dissolved CH_4 can to a high degree be explained by this relationship, due to the high variability in ocean current velocity. That this relationship holds for most of the measuring period also shows that even though observed average concentration are lower in winter months, the seep configuration did not change significantly from July 2015 to May 2016 and dissolved CH_4 was efficiently dispersed in
180 relatively high concentrations in the whole seepage area.

Furthermore, daily CH_4 concentrations at site O_{91} were higher on average than the 24-hour measurements ($313 \text{ vs. } 200 \text{ nmol L}^{-1}$). This can be explained by the comparable measurement periodicity (24 hours) and tidal periodicity (23.93 hours) in the ocean currents, resulting in predominantly eastward advection during daily measurements, thus systematically transferring water from a weak seepage area (Figure 3). We did not observe this effect at site O_{246} , most likely due to less tidal variance
185 in the current direction (Figure 2b). Nonetheless, this systematic tide induced bias on the daily measurements at site O_{91} highlights the importance of taking the oceanographic conditions into account to avoid misinterpretation of variability.

Since currents are mostly northward and seepage are mostly located to the north of both observatories, averaged measured CH_4 concentrations are likely lower than the average over the immediate surrounding area (Figure 3). Despite this, the observatory data show higher average CH_4 concentrations than previously reported. In the area surrounding site O_{91} , Silyakova et al. (2020) reported average concentration of 92, 70, and 61 nmol L^{-1} in June 2014, July 2015, and May 2016, respectively,
190

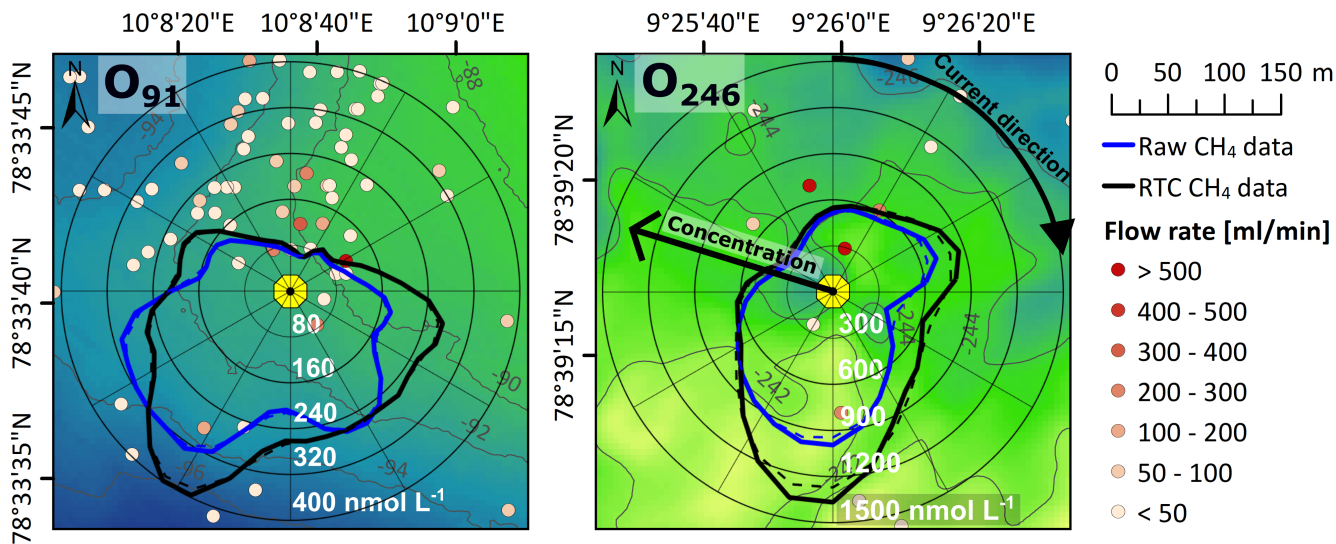


Figure 3. O₉₁ (left) and O₂₄₆ (right) location (yellow dot) as well as flow rates from flares mapped in its vicinity during CAGE 16-4 (colorscale). Background color (green-blue) illustrates seafloor bathymetry. Compass diagram show the relationship between ocean current direction (angle) and CH₄ concentration (distance from center, black is response time corrected (RTC) data and raw data is in blue).

based on discrete water sampling. Averaged CH₄ concentrations measured at site O₉₁ in July 2015 and May 2016 were 566 and 110 nmol L⁻¹ respectively, i.e. around eight and two times higher than values reported by Silyakova et al. (2020). The maximum CH₄ concentration at O₉₁ of 1748±142 nmol L⁻¹ on 20 August 2015 also significantly exceeds the previously maximum recorded concentration in the area of 480 nmol L⁻¹ (July 2014, Silyakova et al., 2020). At site O₂₄₆ the August 2016 average (564 nmol L⁻¹) was eight times higher than what Gentz et al. (2014) found in August 2010 (70 nmol L⁻¹), using an altimeter-controlled CTD towed at 2 meter above the seafloor. Maximum concentration in August 2016 also significantly exceeded previous observations, with 2661±163 nmol L⁻¹ compared to 524 nmol L⁻¹ measured by Gentz et al. (2014).

These differences could be a result of temporal, local or regional differences in CH₄ concentration. However, strong vertical gradients in dissolved CH₄ are well documented at both seep sites (Gentz et al., 2014), and our sensors measured closer to the seafloor (1.2 m above seafloor), compared to Gentz et al. (2014) (2 m above seafloor) and Silyakova et al. (2020) (5 to 15 m above seafloor). Additionally, the observatories were deployed close to seeps using a launcher as opposed to "blind" water sampling from ship-born rosette. Methane was also measured *in situ*, thereby avoiding potential CH₄ outgassing after retrieval of water samples (Schlüter et al., 1998).

Dissolved CH₄ within shallow seep sites where gas can bypass the oceanic sinks often present heterogeneous distribution and rapid temporal variability (Myhre et al., 2016a; Veloso-Alarcón et al., 2019). Our results show that the temporal variability at the two seep sites are higher than previously reported, and that changing ocean currents and configuration of nearby seeps are major contributors. This high short-term variability introduces a conceptual error in studies relying on discrete water sampling

(e.g. to calculate inventories), since the time required to conduct the survey (\sim days) is much longer than large temporal variations in concentration (up to order of 10^3 nmol L⁻¹ within hours).

210 We can obtain a first order constraint on errors caused by short-term variability in a hypothetical water sampling survey using the 24-hour time-series from the observatories. We assume the hypothetical survey seeks to find the average concentration in the bottom layer of the seep site. The expected error can then be found by calculating the standard error of the mean (SEM) for a given number of samples N , using the 24-hour time-series as an underlying distribution representing the sub-daily variability of the seep site (Figure 4, Appendix D contains a detailed outline of the methodology). Even though surveys often require more
215 than 24 hours to complete (2-3 days in Silyakova et al. (2020)), a majority of processes causing short-term variability have periods below or at \sim 24 hours (for instance tides and many turbulent eddies see e.g. Sect. 3.2 and 3.1 and Talley et al. (2011)), likely making the daily distribution relevant also for surveys with longer duration. We compared SEM calculations based on the observatory 24-hour time-series with SEM calculations for the bottom water (\sim 5 meters above the seafloor) discrete water sample data used for average/inventory estimates of the O₉₁ seep site in Silyakova et al. (2020) (also included in Figure 4).

220 The absolute SEM (in nmol L⁻¹) is generally higher for time-series with higher averaged concentrations, making the relative SEM cluster well, with gradually diminishing range for increasing N (an inherent property of the SEM, e.g. 12-45% for $N=10$, 9-30% for $N=30$ etc., Figure 4). The SEM of the data from Silyakova et al. (2020) is similar to the SEM of the 24-hour time-series, with a common range of 5-15% expected error for surveys with $N \sim 60$ samples ($N=64, 62$, and 63 in Silyakova et al. 2020). It should be noted that the comparison with data from Silyakova et al. (2020) has caveats, e.g. that the observatory
225 data does not contain errors due to spatial variability and an assumption of representative short-term temporal variability at the observatory sites (see also Appendix D).

Evidently, detailed surveys of individual seep sites, such as the study by Silyakova et al. (2020), can provide reasonable estimates of local inventories ($<15\%$ uncertainty) despite high short-term temporal variability. However, it is important to note that the area investigated in Silyakova et al. (2020) was densely mapped and homogeneous in the sense that it is an area
230 where seepage is well documented (Silyakova et al., 2020). Interpolation or averaging across larger regions where the amount of seepage is mostly unknown can result in considerable errors due to false interpolation assumptions and amplification of individual measurement errors which can be large (expected errors up to $\sim 140\%$ for single measurements, see listed standard deviations in Figure 4). These effects can potentially explain some of the discrepancies in estimates of oceanic CH₄ inventories and fluxes.

235 Our findings stress the importance of sufficiently dense mapping and knowledge about the underlying seep condition when collecting water samples for inventory estimates. They also highlight the advantage of towed or autonomous instrumentation capable of providing continuous CH₄ data, giving a considerably better coverage and representation of the CH₄ distribution in less time (e.g., Sommer et al., (2015); Grilli et al.(2018); Canning et al., (2021)). Assuming a distribution which better reflects the uneven spread of CH₄ when applying interpolation/extrapolation techniques could also limit estimation errors. Future
240 studies should investigate how initial errors due to short-term and small scale variability propagate via different up-scaling techniques and how these errors can be mitigated.

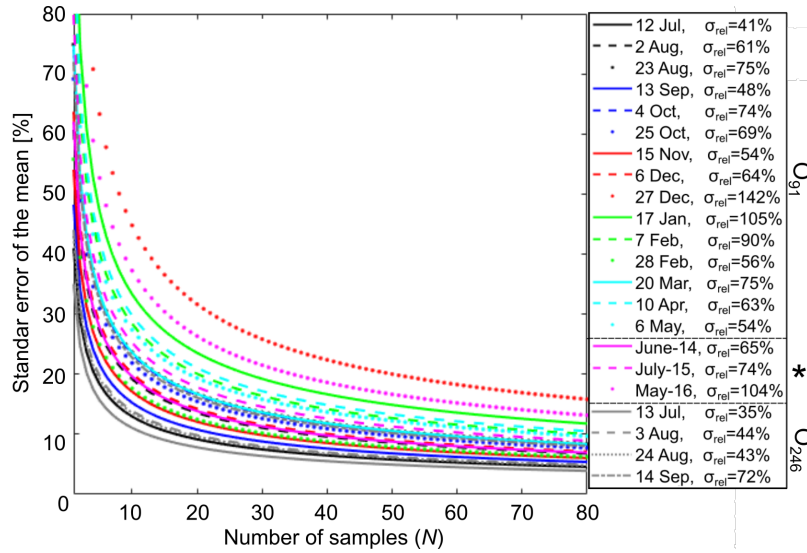


Figure 4. Relative standard error of the mean for different number of samples N for O_{91} 24-hour data (various colors), data presented in Silyakova et al. (2020) (pink lines), and O_{246} 24-hour data (grey lines). Relative standard deviation (corresponding to the standard error with $N=1$) is given in the legend (σ_{rel}). * is data from Silyakova et al. (2020) calculated assuming that the sample distribution resembles the underlying distribution (see Appendix D).

4.2 Hydrostatic pressure

Tidal changes in hydrostatic pressure can trigger CH_4 release by build-up of CH_4 in sediment pore-water at rising tide and subsequent release when pore pressure decreases at falling tide as observed at the Hikurangi Margin (Linke et al., 2009) and Clayoquot slope (Römer et al., 2016). Our study sites differ from these sites in depth (they are >600 m) and in tidal amplitude (4 m at Calyoquot slope compared to 1.5 at PKF). Linke et al., (2010) and Römer et al., (2016) also observed bubbles hydroacoustically, while we measure dissolved CH_4 which is strongly affected by the (also tidally dependent) current direction (Figure 3).

To constrain this effect on CH_4 concentration, we separated the data into overlapping portions depending on the current direction (12° and 30° for O_{91} and O_{246} , respectively) and calculated standard scores of CH_4 concentration for each portion which are less dependent on current direction. We used larger current direction intervals for O_{246} due to the shorter data set. We then binned all the z-scored CH_4 data according to when the data were collected in relation to the M2 governed tidal cycle peak using overlapping 30 minute bins (the M2 tide explains 79.2% and 80.3% of the pressure variance at O_{91} and O_{246} , respectively). Average and median values were then calculated for each bin, giving the averaged/median normalized dissolved CH_4 value (standard score) for each current velocity defined data portion as a function of the M2 tidal cycle (Figure 5). This partial decoupling of variability in hydrostatic pressure and current direction was possible since the bottom water current and

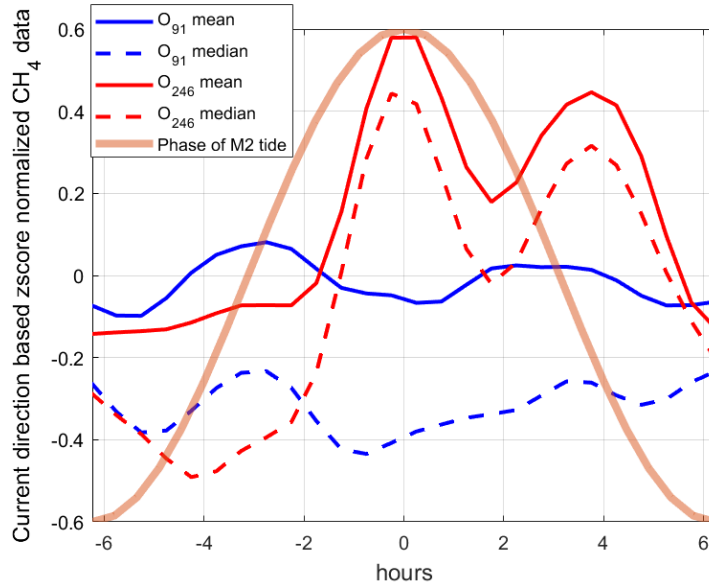


Figure 5. Median and averaged z-scores of CH_4 binned according to bottom water current direction according to where the data were sampled on the phase of the M2 pressure tide.

hydrostatic pressure changes had different dominant tidal constituents, i.e. the current was mainly dominated by the diurnal K1 constituent (~ 23.91 hour period), while the M2 tide is semi-diurnal (12.42 hour period).

A strong effect of the hydrostatic pressure on local seepage should elevate z-scores at decreasing pressure (from 0 to 6.2 hours, i.e. in the right half of Figure 5), which we observe at both observatories. However, we observe stronger peaks at increasing hydrostatic pressure (-3 hours) at site O_{91} and at the M2 peak (0 hours) at site O_{246} , which contradicts this hypothesis. This does not mean that there is no effect of hydrostatic pressure changes, but rather that the seepage in the area is widespread at both falling and rising tide conditions. The high variability caused by the strong effect of current direction also makes it particularly challenging to detect moderate changes in seepage intensity.

265 4.3 Bottom water temperature

Bottom water temperature can affect CH_4 release by altering hydrate stability and CH_4 solubility in pore water and water column (Sloan, 1998; Jansson et al., 2019a). Seasonal CH_4 release variability resulting from temperature variations in the bottom water has been linked to migration of the GHSZ and hydrate dissociation further offshore at ~ 390 m water depth (Berndt et al., 2014; Ferré et al., 2020). Our observatories were deployed in areas too shallow for gas hydrate to form. However, inversely varying seepage intensity between seepage at the GHSZ depth (390 m) and site O_{246} can suggest that these areas are fed by the same hydrocarbon source and that hydrates seasonally block the lateral pathways between these seep sites (Veloso-Alarcón et al., 2019). This is in agreement with the observed long-term (~ 3 months) negative correlation between bottom

water temperature and dissolved CH₄ at site O₂₄₆ (R=-0.31). It should be noted that the same relationship is observed at O₉₁, however no geophysical data are available from this area due to the shallow depth.

275 Tidal pressure variations can affect CH₄ release via pore water solubility (Sect. 4.2), but on longer timescales, CH₄ solubility is almost exclusively a function of water temperature. Higher CH₄ solubility implies more CH₄ dissolved in pore water and within bubble streams, potentially increasing the amount of CH₄ dissolved in bottom water. A small but significant (R=0.33) positive correlation between CH₄ solubility and concentration at site O₂₄₆, and site O₉₁ (considering the same time period, i.e. until 3 October in 2015), could indicate such an effect. This is also an alternative explanation for the negative correlation
280 between temperature and CH₄ concentration at site O₂₄₆.

4.4 Pore water seepage

Short-term temperature increase further offshore (390 m depth) has been linked with release of warm, CH₄ rich fluids from the sediments triggered by short duration seismic events (Franek et al., 2017). This means that increased CH₄ concentration should be accompanied by increased water temperature and reduced salinity due to admixture of warmer, less saline pore
285 water. We compared short-term anomalies (i.e., deviations from daily means) in these three variables in the 24-hour data sets at both seep sites, but found no corroborating evidence for this hypothesis. Instead, the covariance between current velocity and temperature and salinity anomalies indicates that short-term variability is mainly caused by cross-shelf exchange of AW in the WSC and ArW in the CC due to eddies (Hattermann et al., 2016). It also indicates that CH₄ release comes mainly from bubble dissolution and not from pore water seepage.

290 4.5 Seasonal variation of CH₄ distribution at site O₉₁

Low release of CH₄ to the atmosphere from the O₉₁ seep area during summer despite high seabed influx, has been explained by suppression of vertical mixing by strong stratification (Myhre et al., 2016a) or absence of mechanical forcing such as wind stress (Silyakova et al., 2020). However, in fall and winter, the water column offshore PKF is expected to have more horizontal and vertical mixing due to weaker stratification from cooling or sea ice formation (Tverberg et al., 2014), baroclinic instability
295 in the frontal structures of the WSC (von Appen et al., 2016; Hattermann et al., 2016), and more frequent storms (Nilsen et al., 2016).

We expect lower CH₄ variability and lower CH₄ concentration during periods of high mixing and dispersion, due to weaker horizontal and vertical gradients and more efficient dispersion of CH₄ away from sources. We use three sets of parameters to evaluate long term changes in the amount of mixing in the water column (see Appendix E): i) the 4-week averaged bulk
300 velocity shear (S_b), ii) the two dimensional correlation between wind stress and current velocity (R_{WC}), and iii) the number of stormy days defined by persistent winds >11 m/s lasting longer than 6 hours (Figure 6). Calm weather, low S_b and R_{WC} until mid-September 2015 indicate a stable water column with limited mixing in the bottom waters. From mid-September, S_b increased and stayed high until mid-November, together with a gradual increase in R_{WC} which can be attributed to a gradual breakdown of stratification and increasing number of storm events (Figure 6a). R_{WC} remained high ($R_{WC} > 0.5$ at 60 m depth)
305 until March 2016, indicating a significant effect of wind forcing in the water column. From March until observatory retrieval,

R_{WC} decreased to < 0.2 below 50 m depth while S_b increased below 60 m depth, indicating available energy for mixing in the bottom waters.

We quantified CH_4 variability during the 24-hour measurements using the Median Absolute Deviation (MAD) and used the median as a measure of the amount of dissolved CH_4 . The three 24-hour periods collected during the calmer period prior to mid-September had high median concentration (>300 nmol L^{-1}) and the overall highest variability ($MAD > 160$ nmol L^{-1}), as expected for low mixing conditions (Figures 6b and 6c). From mid-September until the end of March (i.e. fall/winter season), the 24-hour CH_4 concentration time-series had generally lower MAD and median concentration. In this period, CH_4 variability and median also showed a good statistical relationship with the 5 days accumulated wind stress ($R = -0.82$ for MAD and $R = -0.61$ for median concentration), indicating that wind forcing has a deep impact on mixing and redistribution of CH_4 in the water column (which also fits well with a high R_{WC}). The two last 24-hour CH_4 time series (10 April and 1 May) had low median concentration, which could be explained by the absence of stratification (Silyakova et al., 2020) and generation of mixing from the observed increase in S_b .

Accumulated wind stress, S_b and R_{WC} are only limited indicators on water column dispersion and mixing. Nonetheless, the relationship between these parameters and the MAD and medians of the 24 hour period CH_4 time series gives a good indication on the seasonal cycle of distribution and vertical transport of CH_4 : strong stratification, less wind forcing and eddy activity in summer limit mixing and prevent CH_4 from reaching the atmosphere. However, in fall and winter, reduced stratification makes the water column more prone to mixing and distribution of CH_4 seems to be strongly linked with wind forcing from September to April.

5 Conclusions

Time-series of dissolved CH_4 at both lander locations show considerably higher CH_4 concentrations (up to 1748 ± 142 nmol L^{-1} at O_{91} and 2727 ± 182 nmol L^{-1} at O_{246}) than previously found in ship-based water sampling surveys (maximum of 482 near O_{91} and of 564 near O_{246}). The time-series also uncover high CH_4 variability (up to ~ 1000 nmol L^{-1}) within short timescales (< 24 hours), highlighting the uncertainty of flux/inventory estimates based on interpolation/extrapolation techniques where even/linear CH_4 distribution is assumed. We calculated the standard error of a mean estimate based on a hypothetical discrete water sampling survey based on a range of samples by using the 24-hour time-series as the underlying distribution. The results aligned well with previous discrete water sampling surveys in the area, giving a standard error of the mean of 5-15% for ~ 60 samples.

Variability can be linked to directional ocean current variations occurring at tidal time-scales which shows the importance of taking the current direction and seep locations into account when interpreting intense seep site observations. The persistent relationship between current direction and location of seeps during recovery shows that there was seepage throughout the year and that the seep configuration was relatively constant.

We did not observe a direct effect of tidal pressure variations on CH_4 release, but this could be hidden by the strong effect of variations in current direction. A negative (long-term) correlation between temperature and dissolved CH_4 at O_{246} is in

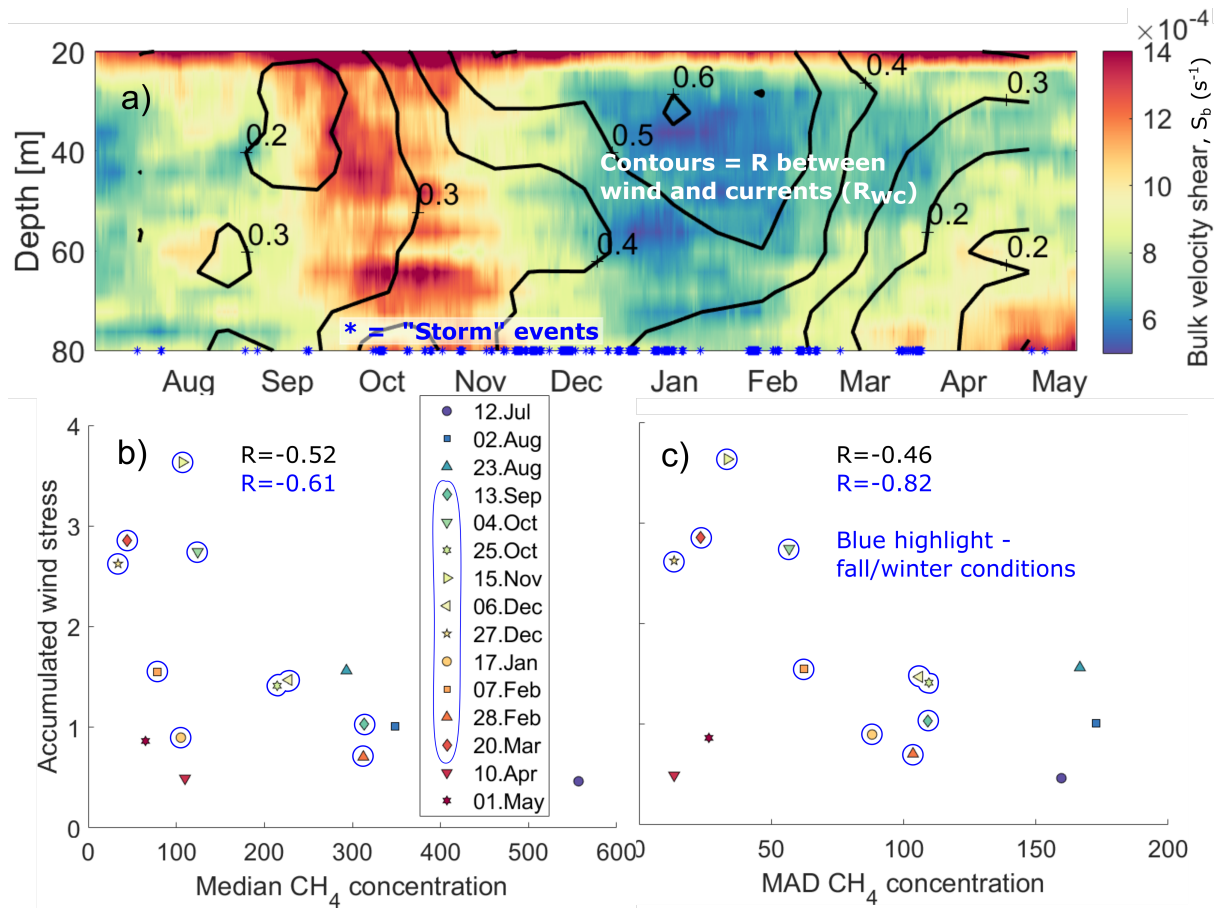


Figure 6. a) Bulk velocity shear ($\Delta H = 8$ meter) and two dimensional correlation with wind stress (contours). Relationships between 5 days accumulated wind stress and median (b) as well as median absolute deviation (c) of CH_4 concentration for 24 hour data periods. Persistent wind events with more than 10 m s^{-1} winds in periods over 6 hours are indicated with blue stars along the x-axis of diagram a). Blue highlights fall/winter water column conditions as described in the text.

agreement with the hypothesized seasonal blocking of lateral CH₄ pathways in the sediments (Veloso-Alarcón et al., 2019) but
340 could also be explained by increased CH₄ solubility in the water column.

Short-term, small-scale variations in temperature and salinity were not linked with increased amounts of dissolved CH₄, but rather with cross-frontal exchange of water masses due to eddies.

We observed a seasonal cycle in the characteristics of the 24-hour time-series which fits with seasonal changes in dispersion and mixing characteristics of the water column. Higher CH₄ concentration and variability in early fall, when stratification
345 was strong, was followed by lower median concentrations and variability in late fall/winter when the water column was more affected by mixing. In late fall/winter, wind forcing was statistically coupled to the concentration and variability of CH₄, probably due to weaker water column stratification.

When estimating the atmospheric impact of a particular CH₄ source based on sparse measurements, it is crucial to have some constraints on the temporal and spatial variability. These constraints can either be direct knowledge about variability itself or
350 how inventory and fluxes are affected by related physical and/or chemical parameters. We observed considerable temporal and spatial variability at the two seep sites which need to be taken into account to obtain meaningful estimates of CH₄ fluxes or inventories. That no strong direct link was found with other oceanographic parameters illustrates the non-linearity of the system, making careful interpretation of measurements important. Future studies should aim to identify the errors that arise via different up-scaling/interpolation techniques, how these errors can be mitigated, and the methodology optimized. Based on
355 our observations, we suggest that uncertainties in CH₄ inventory and seep estimates can be mitigated by taking the local seep configuration, ocean currents and mixing rates into account and employ autonomous instrumentation capable of resolving the steep horizontal gradients in dissolved CH₄. This, alongside direct measurements of seepage by e.g., acoustic instrumentation, can help constrain future estimates of CH₄ flux to the atmosphere from seabed seepage.

Code and data availability. All data presented in this paper can be obtained upon request to the authors and will also be made available
360 in the platform Open research Data at the University of Tromsø – The Arctic University of Norway (<https://dataverse.no/dataverse/uit>). All computer code being used can be obtained upon request to the corresponding author

Appendix A: The K-Lander

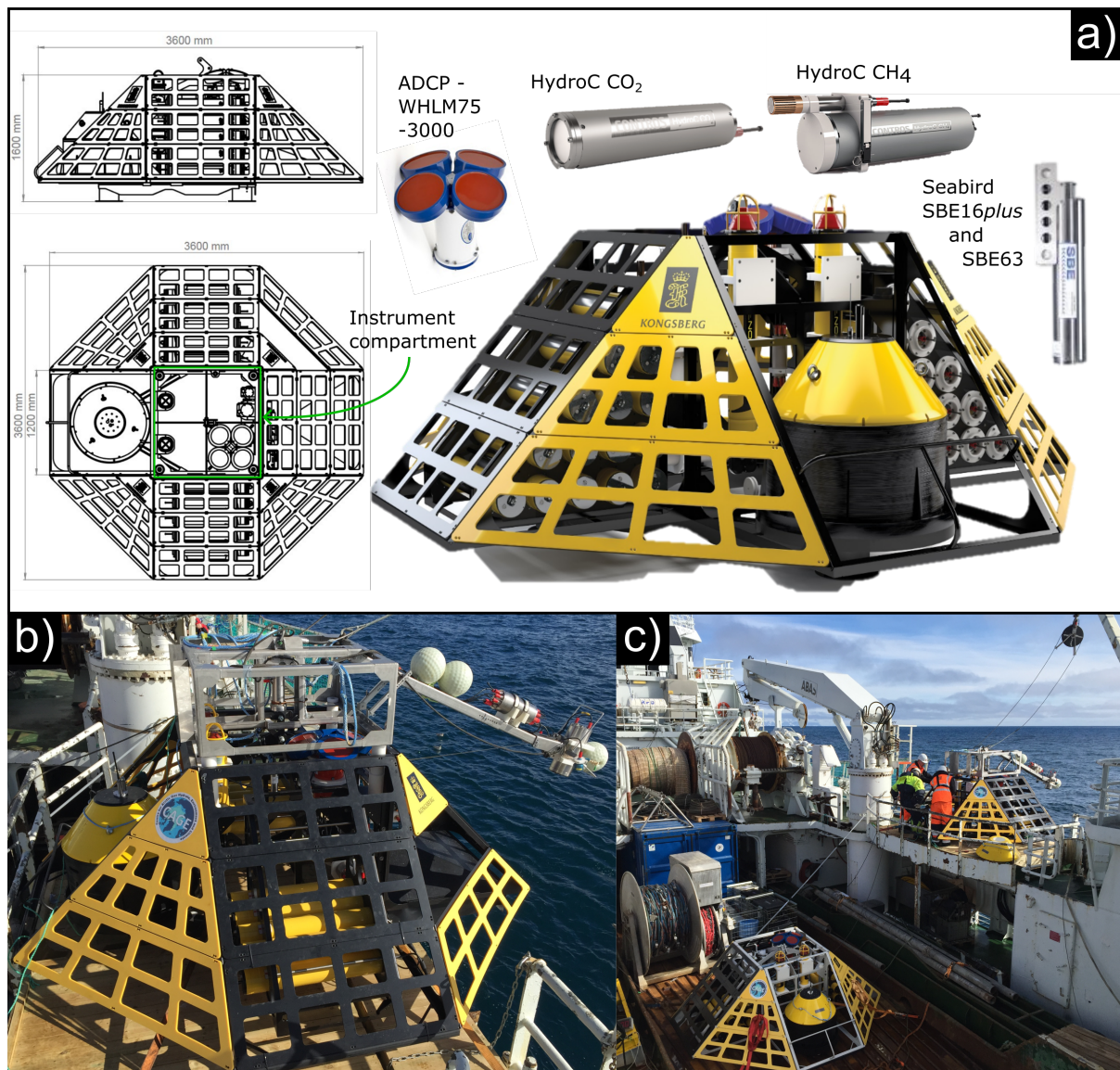


Figure A1. a) The K-Lander is a 1.6 m high and 3.6 m wide trawl-proof stainless-steel frame with multiple instrument mounts and batteries. Side panels are perforated to allow unobstructed water flow to the instruments inside the structure. See Appendix B for details on instrumentation. b) K-Lander during deployment with launcher mounted on top and camera system mounted on a boom for visual control of landing area. c) The two K-landers before deployment.

Appendix B: Measurement intervals, general post-processing and data

365 The CTD/oxygen sensor and ADCP conducted measurements every 4 and 9 minutes, respectively, during the continuous monitoring of CH₄ and CO₂ measurements, and 21 and 29 minutes during the rest of the deployment period (see Table B1 for acronyms, description, and measurement accuracy). Salinity was measured on the practical salinity scale.

370 The upward mounted ADCP measured ocean currents in 1 m bins with a bottom 7 m blank distance, where the topmost 20% of the water column was disregarded due to side lobe interference. The high resolution, relatively short ensemble time (1 minute), and potential presence of CH₄ bubbles in the water resulted in noisy data. We dampened the noise by first removing any data points with error velocities exceeding one short-term (1 week) standard deviation, smoothed the data using a second order Butterworth low-pass filter with a 3-hour cutoff period and a spatial (i.e. vertical) moving average filter with a 5 m Hann window (increasing the blank distance to 10 meter). The accuracy of the ADCP data is therefore not explicitly constrained and is based on comparing current velocity frequency spectra before and after filtering, combined with averaged error velocity of the raw data (Table B1).

Table B1. Instruments mounted on O₉₁ and O₂₄₆ (see Figure A1), measured parameters, height in meters above sea floor (masf) and stated accuracy. ADCP stands for Acoustic Doppler Current Profiler. N shows the number of data-points used for later multi-variable analysis for O₉₁/O₂₄₆. (*)The Contros HydroC CH₄ output partial pressure from the internal gas chamber. (**)We report absolute concentration in seawater (nmol L⁻¹) using Henry's law and (***) report accuracy only for response time corrected (RTC) concentration (see Figure B1) since the accuracy for untreated CH₄ concentration data is ambiguous due to the slow response time.

Instrument	Parameter(s)	masf	N	Accuracy
Teledyne RDI ADCP WHLM75-3000	Current velocity Profile	1.6	17438/4731	~3 cm s ⁻¹
Contros HydroC CH ₄	<i>p</i> CH ₄ (instrument output)* <i>x</i> CH ₄ (reported**)	1.2	1491/281	~ 5-20%(RTC***)
Contros HydroC CO ₂	<i>p</i> CO ₂	1.2	1491/281	N/A (no pump)
SeaBird SBE16 <i>plus</i> V2	Conductivity/Temperature /Depth	1.2	29660/9065	0.0005Sm ⁻¹ /0.005°C, /0.02% of range
Seabird SBE63 oxygen optode	Dissolved Oxygen	1.2	29660/9065	3μmol kg ⁻¹ or ±2%

375 Since sensors were recording at different frequencies, chronological alignment of the data was carried out by identifying nearest neighbor data points or by resampling. For correlation coefficients, histograms, and Fourier analysis, the data sets were resampled to a uniform 15 minute or 1 hour measuring interval depending on the sample frequency of the raw data, using a poly-phase anti-aliasing filter. Due to the power-cycling mode of the CH₄ and CO₂ sensors and differing sampling frequencies, some statistics were based on more data points than others (outlined in Table B1). Daily measurements of CH₄ were excluded
380 from these statistics due to the high probability of systematic errors induced by periodic diurnal effects.

Harmonic analysis of hydrostatic pressure and ocean currents was done using t_{tide} (see Pawlowicz et al., 2002) and the fast Fourier transform.

We calculated the rate of change (ROC) in CH_4 concentration using the response time corrected CH_4 data and the absolute value of the three point (9 minutes) finite differences to limit the effect of noise on the calculation.

385 The absolute concentration of CH_4 in the water (nmol L^{-1}) was estimated from the partial pressure of CH_4 , pressure, temperature, and salinity, using Henry's law and Henry constants obtained from Harvey et al., (1996) and practical molar volume and gamma term from Duan & Mao et al., (2006).

The CH_4 sensors were calibrated to relevant water temperatures prior to deployment. The TDLAS detectors (Contros GmbH, 2016) provide measurements with good selectivity (fit for purpose), high long-term stability (intermittent calibration not necessary), and are unaffected by dissolved oxygen content (unless complete depletion). Biofouling was also minimal at retrieval (due to the cold water and local setting) and the PDMS membranes are almost unaffected by cold water. Generally, we did no observations indicating issues with any of the sensors except for what already mentioned regarding the conductivity probe and electrical malfunction of O_{246} . Furthermore, we discarded all data recorded during instrument warm-up (i.e. when internal temperature was below correct operating temperature), before the individual measurement periods (the instruments were turned 395 on ~ 35 minutes prior to recording the data used in the analysis).

In Contros HydroC CH_4 and CO_2 sensors, dissolved gases diffuse through a hydrophobic membrane into a gas chamber which equilibrate with the ambient environment. This results in a slow response time (e.g. $\tau_{63} \sim 50$ minutes under certain conditions for our membrane and pump setup for the CH_4 sensor) and poor representation of the rapid changes in CH_4 we expected in our study area (Gentz et al., (2013) and Myhre et al., (2016)). We therefore performed a response time correction 400 of the dissolved CH_4 data following the methodology presented in Dølven et al. (2021), modulating the response time using the temperature data (effects of salinity on membrane permeability was not taken into account since these are negligible for the local ranges, see Robb (1968)). The CO_2 sensors had a faulty pump, which ambiguously increased the response time of the sensors making response time correction impossible.

The response time correction was performed for each period individually (1 hour and 24 hour, i.e. 377 periods), using the 405 stated measurement accuracy of the instrument ($2 \mu\text{Atm}$ or 3% of measured value, whichever is higher) as input uncertainty. We first identified the ideal Δt according to the maximum curvature point in the L-curves of the 24 hour measurement periods. These varied slightly between each measurement period, but averaging close to 180 s (176.4 s). To keep the same measuring interval for all the CH_4 data, we therefore corrected all the data with a specified Δt of 180 s, which falls well within the bend of the L-curve and should therefore safeguard a good balance between noise and model error (Figure B1a).

410 The uncertainty estimate varies depending on the amount of CH_4 measured by the TDLAS unit in the measurement chamber of the instrument. The distribution of the uncertainty estimates is shown as percentages in Figure B1b. Estimated uncertainty ranged from 3 to 205 nmol L^{-1} (95% confidence, high for high concentrations in measurement chamber and vice versa) or usually between 5 and 20% although with some outliers when the concentration is low and uncertainty estimate high (Figure B1b).

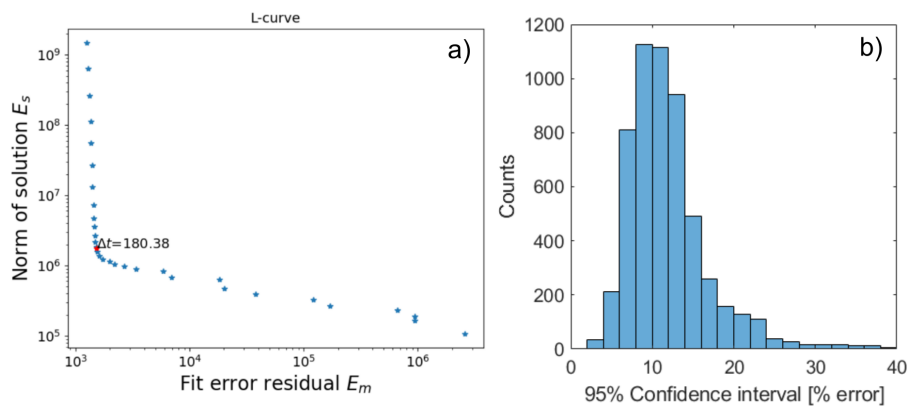


Figure B1. a) L-curve for response time correction of CH₄ data showing the location of the chosen Δt (180 s) for 6 May at O91. b) Estimated relative (percent, %) uncertainty for response time corrected CH₄ data (both observatories).

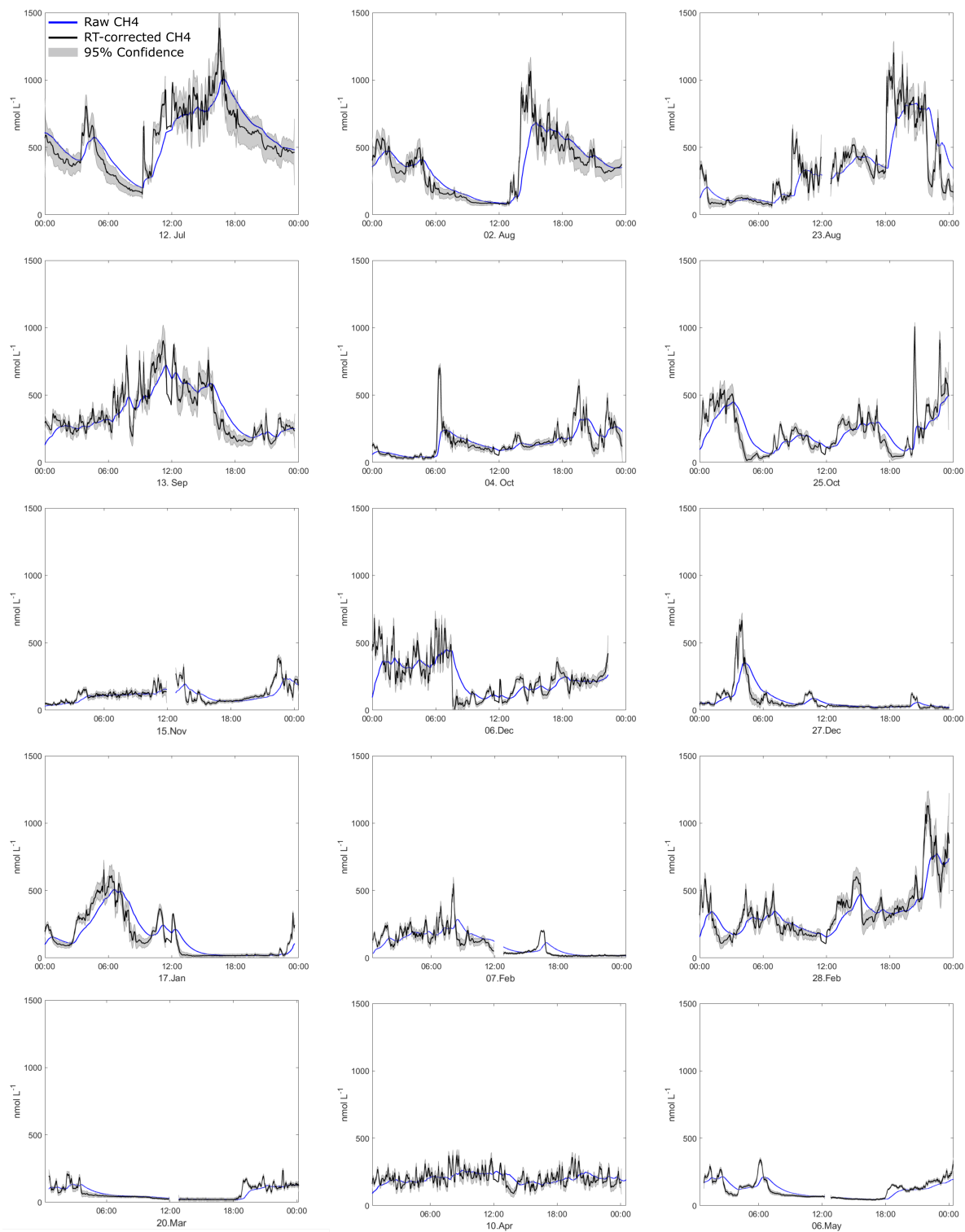


Figure C1. All 24 hour periods of CH₄ concentration at O₉₁ with response time corrected data (black) with uncertainty estimate (grey shade, 95% confidence) and raw data (blue) from O₉₁.

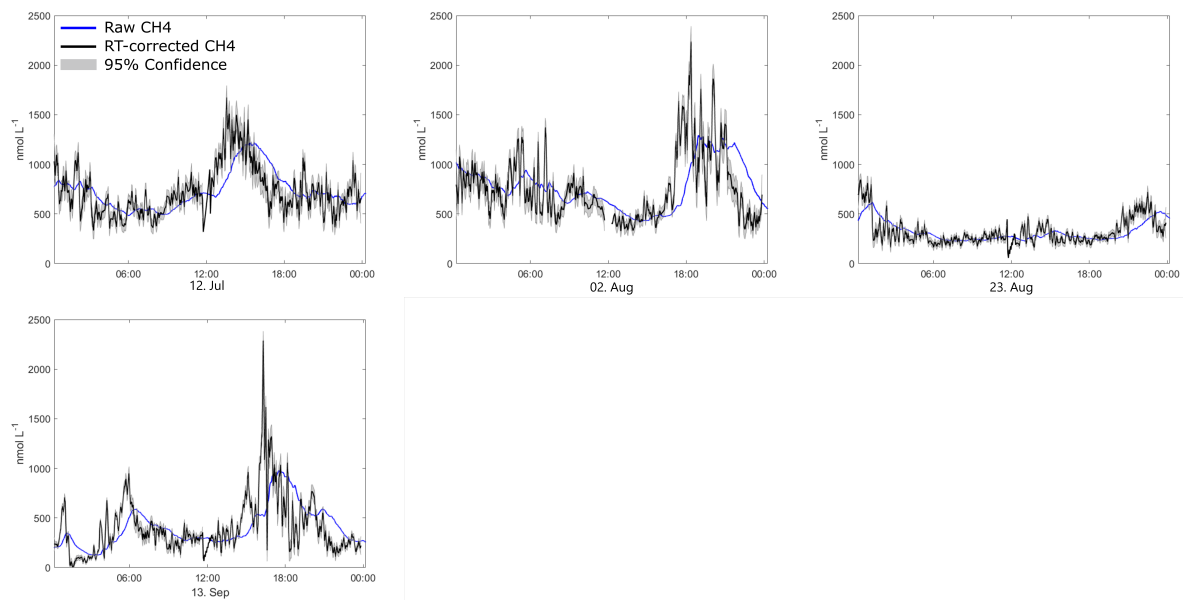


Figure C2. All 24 hour periods of CH₄ concentration at O₂₄₆ with response time corrected data (black) with uncertainty estimate (grey shade, 95% confidence) and raw data (blue) from O₂₄₆.

Appendix D: Standard error of the mean due to temporal variability

To obtain the (theoretical) true dissolved CH₄ average or inventory for an area requires known concentration everywhere at a single point T_0 in time. Considering a hypothetical ship-based discrete water sampling survey, any small scale spatial variability not resolved by the sampling grid or localized (not seep-wide) short-term temporal variability occurring during the survey time
 420 can be considered measurements errors for the purpose of the survey. Assuming that the water samples are sufficiently spaced out to be considered independent samples, the estimated average concentration from N samples in a particular depth layer in a seep site can be expressed as

$$E(m, \epsilon_t, \epsilon_s) = \frac{\sum_{n=1}^N (m + \epsilon_{tn} + \epsilon_{sn})}{N}, \quad (\text{D1})$$

where m is the average of the seep site at T_0 , ϵ_t is errors due to temporal short-term deviation from m at sampling time
 425 $T_0 + \Delta t$ and ϵ_s is spatial deviations in concentration from m . The expected standard error of $E(m, \epsilon_t, \epsilon_s)$ from the short-term temporal/spatial variability is then given by

$$\sigma_{E(m, \epsilon_t, \epsilon_s)} = \frac{\sigma}{\sqrt{N}} \quad (\text{D2})$$

where σ is the standard deviation of the distribution we sample from (see e.g. Ayyub & McCuen, 2003). From Eq. D1 and Eq. D2 we obtain

$$430 \quad \sigma_{E(m, \epsilon_t, \epsilon_s)} = \sigma_{E(m, \epsilon_t)} + \sigma_{E(m, \epsilon_s)} = \frac{\sigma_t}{\sqrt{N}} + \frac{\sigma_s}{\sqrt{N}} \quad (\text{D3})$$

where σ_t and σ_s is the ϵ_t (temporal), and ϵ_s (spatial) variability related standard deviations of the distribution and $\sigma_{E(m, \epsilon_t)}$ and $\sigma_{E(m, \epsilon_s)}$ the corresponding contributions to the standard error of the mean. Assuming the daily variance at the observatory is representative for the seep site, we can describe the expected error caused by sub-daily variability (all ϵ_t) in a scenario where a seep site is being sampled N times using the 24-hour time-series as the underlying distribution. In essence, we treat every
 435 measurement as having an associated probability distribution which is represented by the 24-hour time-series (which gives the sub-daily variability).

In the discrete water sample data presented in Silyakova et al. (2020), the underlying distribution is unknown and we can only assume that the sample distribution resembles the underlying distribution, i.e. that

$$\sigma_{E(m, \epsilon_t, \epsilon_s)} \approx \hat{\sigma}_{E(m, \epsilon_t, \epsilon_s)} = \frac{\sigma_{sampled}}{\sqrt{N}}, \quad (\text{D4})$$

440 where $\hat{\sigma}_{E(m, \epsilon_t, \epsilon_s)}$ is the standard error estimate of the mean based on the sample distribution and $\sigma_{sampled}$ is the standard deviation of the measurements. All three data sets, "June-14" ($N=64$), "July-15" ($N=62$), and "May-16" ($N=63$), have similarly

skewed distribution compared to what is found in the observatory data (see Figure D1), which supports this assumption. The survey in Silyakova et al. (2020) required 2-3 days to complete, while the observatory data only concerns sub-daily variability (24-hour time-series). Nonetheless, we believe the comparison is valid, since the known major contributors to short-term (time-
445 scales below weeks) variability acts on sub-daily scales, such as the dominant frequencies in the ocean currents and pressure changes.

There is a clear relationship of increasing $\sigma_{E(m, \epsilon_t, \epsilon_s)}$ with increasing daily average, making relative $\sigma_{E(m, \epsilon_t, \epsilon_s)}$ a meaningful quantity to use, as opposed to absolute $\sigma_{E(m, \epsilon_t, \epsilon_s)}$. Additionally, for simplicity, we have not differentiated in the notation of the standard error of the mean in the main text of the manuscript, referring to it as simply the standard error of the mean in all
450 situations.

It is also enlightening to consider the distribution of average estimates and how the skewed underlying distribution affects the distribution of average estimate errors for smaller N . We did this by simulating hypothetical surveys by random sampling from the 24-hour data-sets (Figure D2) which shows the elevated probability of underestimating the average for estimates based on few samples ($N \lesssim 30$), i.e. the median error is smaller than the average error. This is caused by an inheritance of the skewed
455 underlying distribution in the CH_4 concentration data (see Figure D2a). This also allows for severe overestimates due to the long right-hand side tail of the distribution. For larger N s ($N \gtrsim 30$), average estimates tend towards being normally distributed, thus avoiding these effects (see Figure D2b).

Error estimates of more complicated properties, such as the total CH_4 content in a volume of water based on interpolation techniques, require an assessment of the individual uncertainties of each measurement and how these errors propagate via e.g.
460 linear interpolation in the spatial domain. While not being explicitly applicable to inventory estimates, the σ_E still describes how random errors cancel out for larger N s in evenly sampled grids, assuming this variability is representative for the seep site.

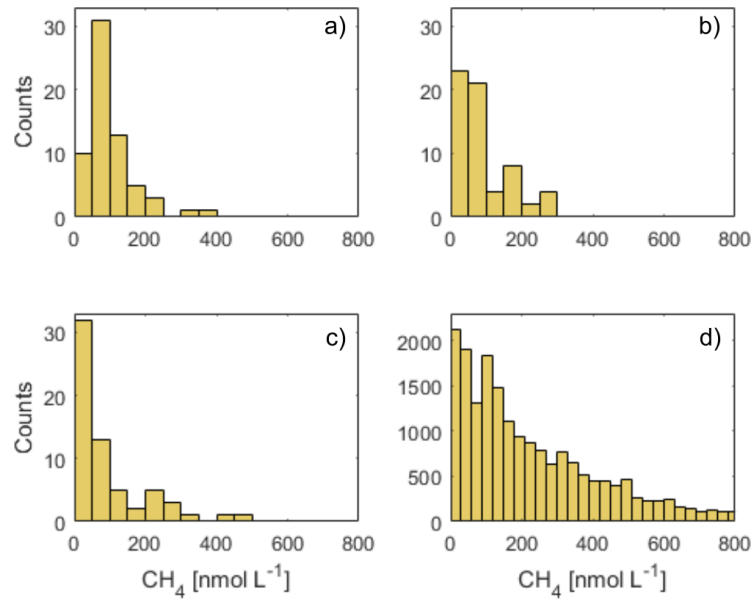


Figure D1. Distribution of CH_4 concentrations from the a) June-14 b) July-15 c) May-16 data in Silyakova et al. (2020) and d) from the 24-hour data (all periods) at O_{91} . Note the different scale for the y-axis between a-c and d.

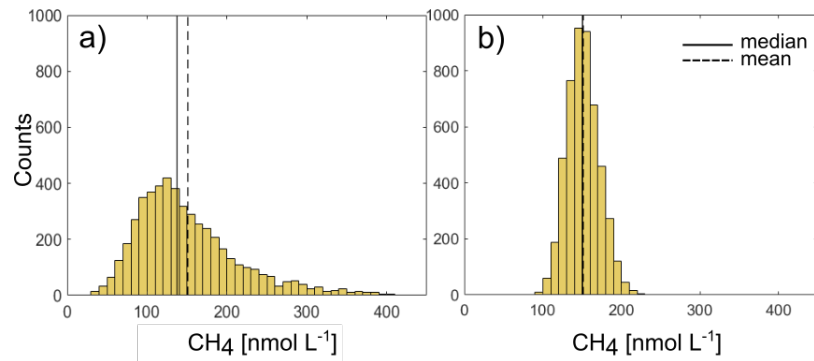


Figure D2. Histograms of simulated average estimates based on $N=10$ (a) and $N=30$ (b) samples from the 24-hour data set from 23 August at O_{91} showing the median and mean as vertical lines.

Appendix E: Bulk velocity shear and wind stress correlation

We calculated bulk wind stress using 10 meter above sea level ERA-interim re-analysis wind data (Dee et al., 2011) and Large & Pond (1981). Water column bulk velocity shear S_b (see e.g. Lincoln et al., 2016) was calculated as

$$S_b^2 = \left(\frac{u_u - u_l}{h_{diff}} \right)^2 + \left(\frac{v_u - v_l}{h_{diff}} \right)^2 \quad (E1)$$

where u_u , u_l , v_u , v_l refer to the easterly and northerly ADCP velocity components in the upper (subscript u) and lower (subscript l) layer and h_{diff} the vertical distance between layers. The direct effect of wind stress is usually confined to surface water, although indirect effects such as Ekman transport/overturning and the formation of eddies can facilitate currents and mixing at deeper depths (Cushman-Roisin and Beckers, 2011). The two-dimensional correlation coefficient R_{WC} between the wind and ocean currents was calculated using Kundu, (1976) and the complex representations τ_c and u_c of the wind stress and de-tided current velocity vectors:

$$R_{WC} = \frac{\langle \tau_c^* u_c \rangle}{\langle \tau_c^* \tau_c \rangle^{\frac{1}{2}} \langle u_c^* u_c \rangle^{\frac{1}{2}}} \quad (E2)$$

where $\langle \dots \rangle$ gives the normalized inner product of the vectors and * annotates the complex conjugate. We allow time-lags up to 15 hours to account for the gradual and indirect effects of wind stress on the ocean currents. Both properties were estimated throughout the valid current velocity profile, but only down to 80 m depth due to the 8 m vertical distance between the defined layers used in the bulk velocity shear calculation.

Author contributions. Conceptualization: KOD,BF,AS,PL,PJ. Data curation: KOD,BF,MM. Formal Analysis: KOD,BF,MM. Funding acquisition: BF. Investigation: KOD, BF, AS. Methodology: KOD,BF. Project administration: BF, AS. Resources: BF. Software: KOD. Supervision: BF. Validation: n/a. Visualization: KOD,MM. Writing - original draft preparation: KOD. Writing - review & editing: KOD, BF, AS, PL, PJ, MM.

Competing interests. The authors declare that they have no conflict of interest.

Acknowledgements. We thank the crew of R/V Helmer Hanssen during the deployment (CAGE 15-3) and recovery (CAGE 16-4) cruises. This study is a part of CAGE (Centre for Arctic Gas Hydrate, Environment and Climate), Norwegian Research Council grant no. 223259). We thank Nicholas Warner for proofreading the article.

References

- Ayyub, B. M. and McCuen, R. H.: Probability, Statistics, and Reliability for Engineers and Scientists, Chapman & Hall/CRC, second edn., 2003.
- Berndt, C., Feseker, T., Treude, T., Krastel, S., Liebetrau, V., Niemann, H., Bertics, V. J., Dumke, I., Dünnbier, K., Ferré, B., Graves, C.,
490 Gross, F., Hissmann, K., Hühnerbach, V., Krause, S., Lieser, K., Schauer, J., and Steinle, L.: Temporal Constraints on Hydrate-Controlled Methane Seepage off Svalbard, *Science*, 343, 284–287, <https://doi.org/10.1126/science.1246298>, 2014.
- Beszczynska-Möller, A., Fahrbach, E., Schauer, U., and Hansen, E.: Variability in Atlantic water temperature and transport at the entrance to the Arctic Ocean, 1997–2010, *ICES Journal of Marine Science*, 69, 852–863, <https://doi.org/10.1093/icesjms/fss056>, 2012.
- Braga, R., Iglesias, R., Romio, C., Praeg, D., Miller, D., Viana, A., and Ketzer, J.: Modelling methane hydrate stability changes and gas
495 release due to seasonal oscillations in bottom water temperatures on the Rio Grande cone, offshore southern Brazil, *Marine and Petroleum Geology*, 112, 104 071, <https://doi.org/https://doi.org/10.1016/j.marpetgeo.2019.104071>, 2020.
- Canning, A., Fietzek, P., Rehder, G., and Körtzinger, A.: Technical note: Seamless gas measurements across the land–ocean aquatic continuum – corrections and evaluation of sensor data for CO₂, CH₄ and O₂ from field deployments in contrasting environments, *Biogeosciences*, 18, 1351–1373, <https://doi.org/10.5194/bg-18-1351-2021>, 2021.
- 500 Contros GmbH: CONTROS HydroC™ CH₄ Sensor for dissolved methane, 2016.
- Cottier, F., Nilsen, F., Inall, M. E., Gerland, S., Tverberg, V., and Svendsen, H.: Wintertime warming of an Arctic shelf in response to large-scale atmospheric circulation, *Geophysical Research Letters*, 34, <https://doi.org/10.1029/2007GL029948>, 2007.
- Cushman-Roisin, B. and Beckers, J.-M.: Introduction to Geophysical Fluid Dynamics, vol. 101, Elsevier Academic Press, second edn., 2011.
- 505 Dee, D., Uppala, S., Simmons, A., Berrisford, P., Poli, P., Kobayashi, S., Andrae, U., Balmaseda, M., Balsamo, G., Bauer, P., Bechtold, P., Beljaars, A., van de Berg, L., Bidlot, J., Bormann, N., Delsol, C., Dragani, R., Fuentes, M., Geer, A., Haimberger, L., Healy, S., Hersbach, H., Hólm, E., Isaksen, I., Kållberg, P., Köhler, M., Matricardi, M., McNally, A., Monge-Sanz, B., Morcrette, J.-J., Park, B.-K., Peubey, C., de Rosnay, P., Tavolato, C., Thépaut, J.-N., and Vitart, F.: The ERA-Interim reanalysis: configuration and performance of the data assimilation system, *Quarterly Journal of the Royal Meteorological Society*, 137, 553–597, <https://doi.org/10.1002/qj.828>, 2011.
- 510 Dølven, K. O., Vierinen, J., Grilli, R., Triest, J., and Ferré, B.: Response time correction of slow response sensor data by deconvolution of the growth-law equation, *Geoscientific Instrumentation, Methods and Data Systems Discussions*, 2021, 1–22, <https://doi.org/10.5194/gi-2021-28>, 2021.
- Duan, Z. and Mao, S.: A thermodynamic model for calculating methane solubility, density and gas phase composition of methane-bearing aqueous fluids from 273 to 523 K and from 1 to 2000 bar, *Geochimica et Cosmochimica Acta*, 70, 3369–3386,
515 <https://doi.org/10.1016/j.gca.2006.03.018>, 2006.
- Etiopie, G., Ciotoli, G., Schwietzke, S., and Schoell, M.: Gridded maps of geological methane emissions and their isotopic signature, *Earth System Science Data*, 11, 1–22, <https://doi.org/10.5194/essd-11-1-2019>, 2019.
- Ferré, B., Mienert, J., and Feseker, T.: Ocean temperature variability for the past 60 years on the Norwegian-Svalbard margin influences gas hydrate stability on human time scales, *Journal of Geophysical Research: Oceans*, 117, <https://doi.org/10.1029/2012JC008300>, 2012.
- 520 Ferré, B., Jansson, P., Moser, M., Portnov, A., Graves, C., Panieri, G., Gründger, F., Berndt, C., Lehmann, M., and Niemann, H.: Reduced methane seepage from Arctic sediments during cold bottom-water conditions, *Nature Geoscience*, 13, 144–148, <https://doi.org/10.1038/s41561-019-0515-3>, 2020.

- Franek, P., Plaza-Faverola, A., Mienert, J., Buenz, S., Ferré, B., and Hubbard, A.: Microseismicity Linked to Gas Migration and Leakage on the Western Svalbard Shelf, *Geochemistry, Geophysics, Geosystems*, 18, 4623–4645, <https://doi.org/10.1002/2017GC007107>, 2017.
- 525 Gentz, T., Damm, E., von Deimling, J. S., Mau, S., McGinnis, D. F., and Schlüter, M.: A water column study of methane around gas flares located at the West Spitsbergen continental margin, *Continental Shelf Research*, 72, 107–118, <https://doi.org/10.1016/j.csr.2013.07.013>, 2014.
- Gerkema, T.: Tidal Constituents and the Harmonic Method, p. 60–86, Cambridge University Press, <https://doi.org/10.1017/9781316998793.005>, 2019.
- 530 Graves, C. A., Lea, S., Gregor, R., Niemann, H., Connely, D. P., Lowry, D., Fisher, R. E., Stott, A. W., Sahling, H., and James, R. H.: Fluxes and fate of dissolved methane released at the seafloor at the landward limit of the gas hydrate stability zone offshore western Svalbard, *Journal of Geophysical Research: Oceans*, 120, 6185–6201, <https://doi.org/10.1002/2015JC011084>, 2015.
- Grilli, R., Triest, J., Chappellaz, J., Calzas, M., Desbois, T., Jansson, P., Guillerm, C., Ferré, B., Lechevallier, L., Ledoux, V., and Romanini, D.: Sub-Ocean: Subsea Dissolved Methane Measurements Using an Embedded Laser Spectrometer Technology, *Environmental Science & Technology*, 52, 10543–10551, <https://doi.org/10.1021/acs.est.7b06171>, 2018.
- 535 Hanson, R. S. and Hanson, T. E.: Methanotrophic bacteria., *Microbiological Reviews*, 1, 439–471, 1996.
- Harvey, A. H.: Semiempirical correlation for Henry’s constants over large temperature ranges, *AIChE Journal*, 42, 1491–1494, <https://doi.org/10.1002/aic.690420531>, 1996.
- Hattermann, T., Erik, I. P., Wilken Jon, A., Jon, A., and Arild, S.: Eddy-driven recirculation of Atlantic Water in Fram Strait, *Geophysical Research Letters*, 43, 3406–3414, <https://doi.org/10.1002/2016GL068323>, 2016.
- 540 Hopkins, T. S.: The GIN Sea—A synthesis of its physical oceanography and literature review 1972–1985, *Earth-Science Reviews*, 30, 175–318, [https://doi.org/https://doi.org/10.1016/0012-8252\(91\)90001-V](https://doi.org/https://doi.org/10.1016/0012-8252(91)90001-V), 1991.
- James, R. H., Bousquet, P., Bussmann, I., Haeckel, M., Kipfer, R., Leifer, I., Niemann, H., Ostrovsky, I., Piskozub, J., Rehder, G., Treude, T., Vielstädte, L., and Greinert, J.: Effects of climate change on methane emissions from seafloor sediments in the Arctic Ocean: A review, *Limnology and Oceanography*, 61, S283–S299, <https://doi.org/https://doi.org/10.1002/lno.10307>, 2016.
- 545 Jansson, P., Ferré, B., Silyakova, A., Dølven, K. O., and Omstedt, A.: A new numerical model for understanding free and dissolved gas progression toward the atmosphere in aquatic methane seepage systems, *Limnology and Oceanography: Methods*, 17, 223–239, <https://doi.org/10.1002/lom3.10307>, 2019a.
- Jansson, P., Triest, J., Grilli, R., Ferré, B., Silyakova, A., Mienert, J., and Chappellaz, J.: High-resolution underwater laser spectrometer sensing provides new insights into methane distribution at an Arctic seepage site, *Ocean Science*, 15, 1055–1069, <https://doi.org/10.5194/os-15-1055-2019>, 2019b.
- 550 Kossel, E., Bigalke, N., Piñero, E., and Haeckel, M.: The SUGAR Toolbox, <https://doi.org/10.1594/PANGAEA.816333>, 2013.
- Kundu, P. K.: Ekman Veering Observed near the Ocean Bottom, *Journal of Physical Oceanography*, 6, 238–242, [https://doi.org/10.1175/1520-0485\(1976\)006<0238:EVONTO>2.0.CO;2](https://doi.org/10.1175/1520-0485(1976)006<0238:EVONTO>2.0.CO;2), 1976.
- 555 Large W. G. and Pond S.: Open Ocean Momentum Flux Measurements in Moderate to Strong Winds, *Journal of Physical Oceanography*, 11, 324–336, [https://doi.org/10.1175/1520-0485\(1981\)011<0324:OOMFMI>2.0.CO;2](https://doi.org/10.1175/1520-0485(1981)011<0324:OOMFMI>2.0.CO;2), 1981.
- Lincoln, B. J., Rippeth, T. P., and Simpson, J. H.: Surface mixed layer deepening through wind shear alignment in a seasonally stratified shallow sea, *Journal of Geophysical Research: Oceans*, 121, 6021–6034, <https://doi.org/https://doi.org/10.1002/2015JC011382>, 2016.
- 560 Linke, P., Sommer, S., Rovelli, L., and McGinnis, D. F.: Physical limitations of dissolved methane fluxes: The role of bottom-boundary layer processes, *Marine Geology*, 272, 209–222, <https://doi.org/10.1016/j.margeo.2009.03.020>, 2009.

- Mau, S., Romer, M., Torres, M. E., Bussmann, I., Pape, T., Damm, E., Geprags, P., Wintersteller, P., Hsu, C.-W., Loher, M., and Bohrmann, G.: Widespread methane seepage along the continental margin off Svalbard - from Bjørnøya to Kongsfjorden, *Scientific Reports*, 7, 42 997, <https://doi.org/10.1038/srep42997>, 2017.
- 565 McDougall, T. J. and Barker, P. M.: Getting started with TEOS-10 and the Gibbs Seawater (GSW) Oceanographic Toolbox, SCOR/IAPSO WG127., p. 22pp, 2011.
- McGinnis, D. F., Greinert, J., Artemov, Y., Beaubien, S. E., and Wüest, A.: Fate of rising methane bubbles in stratified waters: How much methane reaches the atmosphere?, *Journal of Geophysical Research: Oceans*, 111, <https://doi.org/10.1029/2005JC003183>, 2006.
- Myhre, C. L., Ferré, B., Platt, S. M., Silyakova, A., Hermansen, O., Allen, G., Pisso, I., Schmidbauer, N., Stohl, A., Pitt, J., Jansson, P., Greinert, J., Percival, C., Fjaeraa, A. M., O'Shea, S. J., Gallagher, M., Le Breton, M., Bower, K. N., Bauguitte, S. J. B., Dalsøren, S., 570 Vadakkepuliambatta, S., Fisher, R. E., Nisbet, E. G., Lowry, D., Myhre, G., Pyle, J. A., Cain, M., and Mienert, J.: Extensive release of methane from Arctic seabed west of Svalbard during summer 2014 does not influence the atmosphere, *Geophysical Research Letters*, 43, 4624–4631, <https://doi.org/10.1002/2016GL068999>, 2016a.
- Myhre, C. L., Hermansen, O., Fiebig, M., Lunder, C., Fjæraa, A. M., Svendby, T., Platt, M., Hansen, G., Schmidbauer, N., and T., K.: Monitoring of greenhouse gases and aerosols at Svalbard and Birkenes in 2015 - Annual report, NILU report, 31/2016, 2016b.
- 575 Nilsen, F., Skogseth, R., Vaardal-Lunde, J., and Inall, M.: A Simple Shelf Circulation Model: Intrusion of Atlantic Water on the West Spitsbergen Shelf, *Journal of Physical Oceanography*, 46, 1209–1230, <https://doi.org/10.1175/JPO-D-15-0058.1>, 2016.
- Pachauri, R. K. and Meyer, L. A., eds.: IPCC, 2014: Climate Change 2014: Synthesis Report. Contribution of Working Groups I, II and III to the Fifth Assessment Report of the Intergovernmental Panel on Climate Change, IPCC, Geneva, Switzerland, 151 pp, 2014.
- Pawlowicz, R., B., B., and Lentz, S.: Classical Tidal Harmonic Analysis Including Error Estimates in MATLAB using tide, *Computers and 580 Geosciences*, 28, 929–937, 2002.
- Platt, S. M., Eckhardt, S., Ferré, B., Fisher, R. E., Hermansen, O., Jansson, P., Lowry, D., Nisbet, E. G., Pisso, I., Schmidbauer, N., Silyakova, A., Stohl, A., Svendby, T. M., Vadakkepuliambatta, S., Mienert, J., and Lund Myhre, C.: Methane at Svalbard and over the European Arctic Ocean, *Atmospheric Chemistry and Physics*, 18, 17 207–17 224, <https://doi.org/10.5194/acp-18-17207-2018>, 2018.
- Portnov, A., Vadakkepuliambatta, S., Mienert, J., and Hubbard, A.: Ice-sheet-driven methane storage and release in the Arctic, *Nature 585 Communications*, 7, 10 314, <https://doi.org/10.1038/ncomms10314>, 2016.
- Rajan, A., Mienert, J., and Bünz, S.: Acoustic evidence for a gas migration and release system in Arctic glaciated continental margins offshore NW-Svalbard, *Marine and Petroleum Geology*, 32, 36–49, <https://doi.org/10.1016/j.marpetgeo.2011.12.008>, 2012.
- Reagan, M. T., Moridis, G. J., Elliott, S. M., and Maltrud, M.: Contribution of oceanic gas hydrate dissociation to the formation of Arctic Ocean methane plumes, *Journal of Geophysical Research: Oceans*, 116, <https://doi.org/10.1029/2011JC007189>, 2011.
- 590 Reeburgh, W. S.: Oceanic Methane Biogeochemistry, *Chemical Reviews*, 107, 486–513, <https://doi.org/10.1021/cr050362v>, 2007.
- Robb, W. L.: Thin silicone membranes - Their permeation properties and some applications, *Annals of the New York Academy of Sciences*, 146, 119–137, <https://doi.org/10.1111/j.1749-6632.1968.tb20277.x>, 1968.
- Römer, M., Riedel, M., Scherwath, M., Heesemann, M., and Spence, G. D.: Tidally controlled gas bubble emissions: A comprehensive study using long-term monitoring data from the NEPTUNE cabled observatory offshore Vancouver Island, *Geochemistry, Geophysics, 595 Geosystems*, 17, 3797–3814, <https://doi.org/10.1002/2016GC006528>, 2016.
- Ruppel, C. and Kessler, J.: The interaction of climate change and methane hydrates, *Reviews of Geophysics*, 55, 126–168, <https://doi.org/10.1002/2016RG000534>, 2017.

- Sahling, H., Römer, M., Pape, T., Bergès, B., dos Santos Ferreira, C., Boelmann, J., Geprägs, P., Tomczyk, M., Nowald, N., Dimmler, W., Schroedter, L., Glockzin, M., and Bohrmann, G.: Gas emissions at the continental margin west of Svalbard: mapping, sampling, and quantification, *Biogeosciences*, 11, 6029–6046, <https://doi.org/10.5194/bg-11-6029-2014>, 2014.
- 600 Saloranta, T. M. and Svendsen, H.: Across the Arctic front west of Spitsbergen: high-resolution CTD sections from 1998-2000, *Polar Research*, 20, 177–184, <https://doi.org/10.1111/j.1751-8369.2001.tb00054.x>, 2001.
- Sarkar, S., Berndt, C., Minshull, T. A., Westbrook, G. K., Klaeschen, D., Masson, D. G., Chabert, A., and Thatcher, K. E.: Seismic evidence for shallow gas-escape features associated with a retreating gas hydrate zone offshore west Svalbard, *Journal of Geophysical Research: Solid Earth*, 117, <https://doi.org/10.1029/2011JB009126>, 2012.
- 605 Saunois, M., Jackson, R. B., Bousquet, P., Poulter, B., and Canadell, J. G.: The growing role of methane in anthropogenic climate change, *Environmental Research Letters*, 11, 120207, <https://doi.org/10.1088/1748-9326/11/12/120207>, 2016.
- Saunois, M., R. Stavert, A., Poulter, B., Bousquet, P., G. Canadell, J., B. Jackson, R., A. Raymond, P., J. Dlugokencky, E., Houweling, S., K. Patra, P., Ciais, P., K. Arora, V., Bastviken, D., Bergamaschi, P., R. Blake, D., Brailsford, G., Bruhwiler, L., M. Carlson, K., Carrol, M., 610 Castaldi, S., Chandra, N., Crevoisier, C., M. Crill, P., Covey, K., L. Curry, C., Etiope, G., Frankenberg, C., Gedney, N., I. Hegglin, M., Höglund-Isaksson, L., Hugelius, G., Ishizawa, M., Ito, A., Janssens-Maenhout, G., M. Jensen, K., Joos, F., Kleinen, T., B. Krummel, P., L. Langenfelds, R., G. Laruelle, G., Liu, L., MacHida, T., Maksyutov, S., C. McDonald, K., McNorton, J., A. Miller, P., R. Melton, J., Morino, I., Müller, J., Murguia-Flores, F., Naik, V., Niwa, Y., Noce, S., O'Doherty, S., J. Parker, R., Peng, C., Peng, S., P. Peters, G., Prigent, C., Prinn, R., Ramonet, M., Regnier, P., J. Riley, W., A. Rosentretter, J., Segers, A., J. Simpson, I., Shi, H., J. Smith, S., Paul Steele, L., F. Thornton, B., Tian, H., Tohjima, Y., N. Tubiello, F., Tsuruta, A., Viovy, N., Voulgarakis, A., S. Weber, T., Van Weele, M., R. Van Der Werf, G., F. Weiss, R., Worthy, D., Wunch, D., Yin, Y., Yoshida, Y., Zhang, W., Zhang, Z., Zhao, Y., Zheng, B., Zhu, Q., Zhu, Q., and Zhuang, Q.: The global methane budget 2000-2017, *Earth System Science Data*, 12, 1561–1623, <https://doi.org/10.5194/essd-12-1561-2020>, 2020.
- 615 Schlüter, M., Linke, P., and Suess, E.: Geochemistry of a sealed deep-sea borehole on the Cascadia Margin, *Marine Geology*, 148, 9–20, [https://doi.org/https://doi.org/10.1016/S0025-3227\(98\)00016-4](https://doi.org/https://doi.org/10.1016/S0025-3227(98)00016-4), 1998.
- 620 Shakhova, N., Semiletov, I., Leifer, I., Salyuk, A., Rekant, P., and Kosmach, D.: Geochemical and geophysical evidence of methane release over the East Siberian Arctic Shelf, *Journal of Geophysical Research: Oceans*, 115, <https://doi.org/10.1029/2009JC005602>, 2010.
- Silyakova, A., Jansson, P., Serov, P., Ferré, B., Pavlov, A. K., Hattermann, T., Graves, C. A., Platt, S. M., Myhre, C. L., Gründger, F., and Niemann, H.: Physical controls of dynamics of methane venting from a shallow seep area west of Svalbard, *Continental Shelf Research*, 194, 104030, <https://doi.org/https://doi.org/10.1016/j.csr.2019.104030>, 2020.
- 625 Sloan, E. D.: Physical/chemical properties of gas hydrates and application to world margin stability and climatic change, *Geological Society, London, Special Publications*, 137, 31–50, 1998.
- Sommer, S., Schmidt, M., and Linke, P.: Continuous inline mapping of a dissolved methane plume at a blowout site in the Central North Sea UK using a membrane inlet mass spectrometer – Water column stratification impedes immediate methane release into the atmosphere, *Marine and Petroleum Geology*, 68, 766–775, <https://doi.org/10.1016/j.marpetgeo.2015.08.020>, 2015.
- 630 Steinle, L., Graves, C., Treude, T., Ferre, B., Biastoch, A., Bussmann, I., Berndt, C., Krastel, S., James, R., Behrens, E., Böning, C., Greinert, J., Sapart, C., Scheinert, M., Sommer, S., Lehmann, M., and Niemann, H.: Water column methanotrophy controlled by a rapid oceanographic switch, *Nature Geoscience*, 8, 378–382, <https://doi.org/10.1038/NGEO2420>, 2015.
- Talley, L. D., Pickard, G. L., Emery, W. J., and Swift, J. H.: Chapter 1 - Introduction to Descriptive Physical Oceanography, in: *Descriptive Physical Oceanography (Sixth Edition)*, edited by Talley, L. D., Pickard, G. L., Emery, W. J., and Swift, J. H., pp. 1–6, Academic Press, 635 Boston, sixth edition edn., <https://doi.org/https://doi.org/10.1016/B978-0-7506-4552-2.10001-0>, 2011.

- Tverberg, V., Nøst, O. A., Lydersen, C., and Kovacs, K. M.: Winter sea ice melting in the Atlantic Water subduction area, Svalbard Norway, *Journal of Geophysical Research: Oceans*, 119, 5945–5967, <https://doi.org/10.1002/2014JC010013>, 2014.
- Veloso, M., Greinert, J., Mienert, J., and Batist, M.: A new methodology for quantifying bubble flow rates in deep water using splitbeam echosounders: Examples from the Arctic offshore NW-Svalbard, *Limnology and Oceanography: Methods*, 13, 267–287, 2015.
- 640 Veloso-Alarcón, M. E., Jansson, P., Batist, M. D., Minshull, T. A., Westbrook, G. K., Pälike, H., Bünz, S., Wright, I., and Greinert, J.: Variability of Acoustically Evidenced Methane Bubble Emissions Offshore Western Svalbard, *Geophysical Research Letters*, 46, 9072–9081, <https://doi.org/10.1029/2019GL082750>, 2019.
- von Appen, W.-J., Schauer, U., Hattermann, T., and Beszczynska-Möller, A.: Seasonal Cycle of Mesoscale Instability of the West Spitsbergen Current, *Journal of Physical Oceanography*, 46, 1231–1254, <https://doi.org/10.1175/JPO-D-15-0184.1>, 2016.
- 645 Westbrook, G. K., Thatcher, K. E., Rohling, E. J., Piotrowski, A. M., Pälike, H., Osborne, A. H., Nisbet, E. G., Minshull, T. A., Lanoisellé, M., James, R. H., Hühnerbach, V., Green, D., Fisher, R. E., Crocker, A. J., Chabert, A., Bolton, C., Beszczynska-Möller, A., Berndt, C., and Aquilina, A.: Escape of methane gas from the seabed along the West Spitsbergen continental margin, *Geophysical Research Letters*, 36, <https://doi.org/10.1029/2009GL039191>, 2009.